7. Morin, P. *et al*. Activation of β-catenin-Tcf signaling in colon cancer by mutations in β-catenin or APC. *Science* **275,** 1787–1790 (1997).
8. Rubinfeld, B. *et al*. Stabilization of β-catenin by genetic defects in melanoma cell lines. *Science* **275,** 1790–1792 (1997).
9. Akimura, H. *et al*. *Drosophila* CBP is a co-activator of *cubitus interruptus* in *hedgehog* signalling. *Nature* **386,** 735–738 (1997).
10. Akimura, H., Hou, D.-X. & Ishii, S. *Drosophila* CBP is required for *dorsal*-dependent *twist* gene expression. *Nature Genet.* **17,** 211–214 (1997).
11. Chivria, J. C. *et al*. Phosphorylated CREB binds specifically to the nuclear protein CBP. *Nature* **365,** 855–859 (1993).
12. Goldman, P. S., Tran, V. K. & Goodman, R. H. The multifunctional role of the co-activator CBP in transcriptional regulation. *Recent Prog. Horm. Res.* **52,** 103–119 (1997).
13. Bannister, A. J. & Kouzarides, T. CBP-induced stimulation of c-Fos activity is abrogated by E1A. *EMBO J.* **14,** 4758–4762 (1995).
14. Eresh, S., Riese, J., Jackson, D. B., Bohmann, D. & Bienz, M. A CREB binding site as a target for *decapentaplegic* signalling during *Drosophila* endoderm induction. *EMBO J.* **16,** 2014–2022 (1997).
15. Riese, J., Tremml, G. & Bienz, M. D-Fos, a target gene of Decapentaplegic signalling with a critical role during *Drosophila* endoderm induction. *Development* **124,** 3353–3361 (1997).
16. Perrimon, N. The genetic basis for patterned baldness in *Drosophila*. *Cell* **76,** 781–784 (1994).
17. Immerglück, K., Lawrence, P. A. & Bienz, M. Induction across germ layers in *Drosophila* mediated by a genetic cascade. *Cell* **62,** 261–268 (1990).
18. Hoppler, S. & Bienz, M. Two different thresholds of *wingless* signalling with distinct development consequences in the *Drosophila* midgut. *EMBO J.* **14,** 5016–5026 (1995).
19. Yu, X., Hoppler, S., Eresh, S. & Bienz, M. *decapentaplegic*, a target gene of the *wingless* signalling pathway in the *Drosophila* midgut. *Development* **122,** 849–858 (1996).
20. Siegfried, E., Chou, T. B. & Perrimon, N. *wingless* signaling acts through *zeste-white 3*, the *Drosophila* homolog of glycogen synthase kinase-3, to regulate *engrailed* and establish cell fate. *Cell* **71,** 1167–1179 (1992).
21. Szüts, D., Freeman, M. & Bienz, M. Antagonism between EGFR and Wingless signalling in the larval cuticle of *Drosophila*. *Development* **124,** 3209–3219 (1997).
22. Sanson, B., White, P. & Vincent, J.-P. Uncoupling cadherin-based adhesion from *wingless* signalling in *Drosophila*. *Nature* **383,** 627–630 (1996).
23. Ogryzko, V. V., Schiltz, R. L., Russanova, V., Howard, B. H. & Nakatani, Y. The transcriptional coactivators p300 and CBP are histone acetyltransferases. *Cell* **87,** 953–959 (1996).
24. Bannister, A. J. & Kouzarides, T. The CBP co-activator is a histone acetyltransferase. *Nature* **384,** 641–643 (1996).
25. Imhof, A. *et al*. Acetylation of general transcription factors by histone acetyltransferases. *Curr. Biol.* **7,** 689–692 (1997).
26. Gu, W. & Roeder, R. G. Activation of p53 sequence-specific DNA binding by acetylation of the p53 C-terminal domain. *Cell* **90,** 595–606 (1997).
27. Peifer, M., Sweeton, D., Casey, M. & Wieschaus, E. wingless signal and Zeste-white 3 kinase trigger opposing changes in the intracellular distribution of Armadillo. *Development* **120,** 369–380 (1994).
28. Muraoka, M. *et al*. p300 gene alterations in colorectal and gastric carcinomas. *Oncogene* **12,** 1565–1569 (1996).
29. Brand, A. H. & Perrimon, N. Targeted gene expression as a means of altering cell fates and generating dominant phenotypes. *Development* **118,** 401–415 (1993).

Supplementary information is available on *Nature*'s World-Wide Web site (http://www.nature.com) or as paper copy from the London editorial office of *Nature*.

Acknowledgements. We thank S. Ishii for *nej* mutants and plasmids; X. Yu, S. Greaves and J.-P. Vincent for strains and for sharing unpublished results; D. Owen for synthetic peptides; T. Kouzarides and R. Grosschedl for plasmids; M. Peifer and P. Simpson for fly strains; and X. Yu, M. Freeman and H. Pelham for discussion. L.W. is supported by an EMBO long-term fellowship.

Correspondence and requests for materials should be addressed to M.B. (e-mail: mb2@mrc-lmb.cam.ac.uk).

correction

Role of HIF-1α in hypoxia-mediated apoptosis, cell proliferation and tumour angiogenesis

Peter Carmeliet, Yuval Dor, Jean-Marc Herbert, Dai Fukumura, Koen Brusselmans, Mieke Dewerchin, Michal Neeman, Françoise Bono, Rinat Abramovitch, Patrick Maxwell, Cameron J. Koch, Peter Ratcliffe, Lieve Moons, Rakesh K. Jain, Désiré Collen & Eli Keshert

Nature **394,** 485–490 (1998)

The last author's name was misspelled but is now corrected above.

Also, in the penultimate sentence of the introductory bold paragraph, growth was accelerated in HIF-1$\alpha^{-/-}$ tumours (not in HIF-1α tumours, as published). □

Tests of quantum gravity from observations of γ-ray bursts

G. Amelino-Camelia, John Ellis, N. E. Mavromatos, D. V. Nanopoulos & Subir Sarkar

Nature **393,** 763–765 (1998)

In ref. 22 of this Letter, the first author's name was incorrectly cited as C. L. Bhat instead of P. N. Bhat. □

erratum

Perinuclear localization of chromatin facilitates transcriptional silencing

Erik D. Andrulis, Aaron M. Neiman, David C. Zappulla & Rolf Sternglanz

Nature **394,** 592–595 (1998)

Owing to an error in the production process, the six bottom panels of Fig. 1 reproduced poorly. The figure is shown again here. □

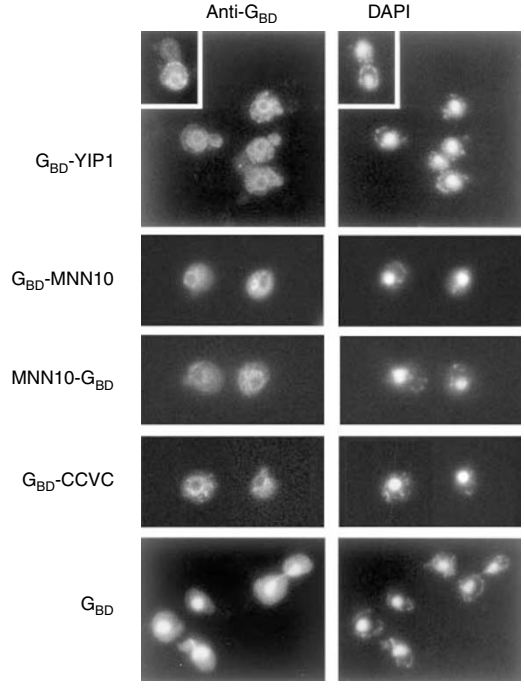

subsequently in dengue, HIV and malaria infections[15–17]. This concept translates readily into current models of presentation of APL to CTLs, leading to segregation of functions through differential signals[18,19]. Thymocytes receiving such a signal may be positively selected[20] and it is possible that encounters of a similar nature may also provoke CTL expansion in the periphery, particularly in a situation, where, as here, primed CTLs are present in excess over naive precursors. A huge expansion of antigen-specific CTLs occurs in LCMV which persist and may be re-expanded during the memory phase[21–23]. This re-expansion is antigen-specific, but the effect of variant antigens has not previously been explored and such effects may be relevant in emerging HIV, HBV and HCV variants[2,24–27]. In the LCMV model used here, this phenomenon was seen in a range of variants arising in mice with monoclonal or polyclonal CTL repertoires, and under a variety of infection conditions. Although adaptability is a dominant feature of the normal immune response, highly mutable viruses may, in a finely tailored way, be testing its limits[28]. □

Methods

CTLs were prepared from spleens of intravenously infected C57BL/6 and BALB/c mice, and used either directly or after 5 days restimulation *in vitro*, in chromium release assays[3]. Virus stocks used here LCMV-WE (from F. Lehmann-Grube), LCMV-Docile (from C. Pfau) and LCMV-Armstrong (from M. Buchmeier). For *ex vivo* lysis assays, splenocytes were collected 8 d after acute infection and 4 d after rechallenge (2×10^6 PFU) and used directly in CTL assays[29]. Challenge with recombinant vaccinia virus was with 2×10^6 PFU i.p. Results are from pooled spleens from 2 mice at a fixed effector:target (E:T) ratio of 50:1 in the case of peptide titrations, and means of 2–3 individual mice in the case of E:T titrations: a representative experiment from 2–3 experiments is shown in each case. Peptides were prepared by solid-phase synthesis (Neosystem, Strasbourg, France). EL4 cells, P815 and MC57G cells were prepulsed at 10–100 nM for use in CTL assays or *in vitro* restimulation. For *in vitro* restimulation, splenocytes from C57BL/6 memory mice stimulated with an irrelevant D^b-restricted peptide derived from adenovirus (SGPSNTPPEI), or from BALB/c memory mice stimulated with an irrelevant L^d-restricted peptide derived from MCMV (YPHFMPTNL), did not generate lytic responses above background level. Virus was titrated by immunological focus assay[30] and cDNA was sequenced as before[13]. Recombinant vaccinia viruses Vac-G2 and Vac-YN4 were kindly provided by D. Bishop.

Received 11 February; accepted 28 May 1998.

1. Phillips, R. E. *et al.* Human immunodeficiency virus genetic variation that can escape cytotoxic T cell recognition. *Nature* **354,** 453–459 (1991).
2. Bertoletti, A. *et al.* Cytotoxic T lymphocyte resonse to a wild type hepatitis B virus epitope in patients chronically infected by variant viruses carrying substitutions within the epitope. *J. Exp. Med.* **180,** 933–943 (1994).
3. Pircher, H. *et al.* Viral escape by selection of cytotoxic T cell-resistant variants *in vivo*. *Nature* **346,** 629–233 (1990).
4. Bertoletti, A. *et al.* Natural variants of cytotoxic epitopes are T-cell receptor antagonists for antiviral cytotoxic T cells. *Nature* **369,** 407–410 (1994).
5. Klenerman, P. *et al.* Naturally occurring HIV-1 *gag* variants antagonize cytotoxic T-cell activity. *Nature* **369,** 403–406 (1994).
6. Francis, T. Influenza: The newe acquayantance. *Ann. Intern. Med.* **39,** 203–212 (1953).
7. De St Groth, F. & Webster, R. Disquisitions on original antigenic sin. I. Evidence in man. *J. Exp. Med.* **124,** 331–345 (1966).
8. De St Groth, F. & Webster, R. Disquisitions on original angigenic sin. II. Proof in lower creatures. *J. Exp. Med.* **124,** 347–361 (1966).
9. Hotchin, J. The biology of LCMV infection: Virus induced immune disease. *Cold Spring Harbor Symp. Quant. Biol.* **27,** 470–488 (1962).
10. Aebischer, T., Moskophidis, D., Rohrer, U. H., Zinkernagel, R. M. & Hengartner, H. *In vitro* selection of lymphocytic choriomeningitis virus escape mutants by cytotoxic T lymphocytes. *Proc. Natl Acad. Sci. USA* **88,** 11047–11051 (1991).
11. Moskophidis, D. & Zinkernagel, R. M. Immunobiology of cytotoxic T-cell escape mutants of lymphocytic choriomeningitis virus. *J. Virol.* **69,** 2187–2193 (1995).
12. Jacobson, S. & Pfau, C. Viral pathogenesis and resistance to defective interfering particles. *Nature* **283,** 311–315 (1980).
13. Klenerman, P., Hengartner, H. & Zinkernagel, R. A non-retroviral RNA virus persists in DNA form. *Nature* **390,** 298–301 (1997).
14. Lewicki, H. *et al.* CTL escape variants. 1. Generation and molecular characterization. *Virology* **210,** 29–40 (1995).
15. Good, M., Zevering, Y., Currier, J. & Bilsborough, J. Original antigenic sin, T cell memory and malaria sporozoite immunity: an hypothesis for immune evasion. *Parasite Immunol.* **15,** 187–193 (1993).
16. Halstead, S., Rojanasuphot, S. & Tsurukubo, Y. Original antigenic sin in dengue. *Am. J. Hyg. Trop. Med.* **32,** 154–156 (1983).
17. Nara, P. L. *et al.* Emergence of viruses resistant to neutralization by V3-specific antibodies in experimental human immunodeficiency virus type 1 IIIB infection of chimpanzees. *J. Virol.* **64,** 3779–3791 (1990).
18. Evavold, B. & Allen, P. Separation of IL-4 production from proliferation by an altered peptide ligand. *Science* **252,** 1308–1310 (1991).
19. Kessler, B., Bassanini, P., Cerottini, J. & Luescher, I. Effects of epitope modificaiton on TCR ligand binding and antigen recognition by seven H-$2K^d$ restricted CTL clones specific for a photoreactive peptide derivative. *J. Exp. Med.* **185,** 629–640 (1997).
20. Jameson, S. C. & Bevan, M. J. T cell receptor antagonists and partial agonists. *Immunity* **2,** 1–11 (1995).
21. Butz, E. & Bevan, M. Massive expansion of antigen-specific CD8+ cells during acute virus infection. *Immunity* **8,** 167–175 (1998).
22. Murali-Krishna, K. *et al.* Counting antigen-specific CD8 T cells: a reevaulation of bystander activation during viral infection. *Immunity* **8,** 177–187 (1998).
23. Gallimore, A. *et al.* Induction and exhaustion of LCMV-specific CTL visualised using soluble tetrameric MHC–peptide complexes. *J. Exp. Med.* **187,** 1383–1393 (1998).
24. Klenerman, P., Meier, U. C., Phillips, R. E. & McMichael, A. J. The effects of natural altered peptide ligands on the whole blood cytotoxic T lymphocyte response to human immunodeficiency virus. *Eur. J. Immunol.* **25,** 1927–1931 (1995).
25. McAdam, S. N. *et al.* Immunogenic HIV variants that bind to HLA-B8 but fail to stimulate CTL responses. *J. Immunol.* **155,** 2729–2736 (1995).
26. Weiner, D. *et al.* Persistent hepatitis C virus infection in a chimpanzee is associated with emergence of a CTL escape variant. *Proc. Natl Acad. Sci. USA* **82,** 2755–2759 (1995).
27. Kent, S., Greenberg, P., Hoffman, M., Akridge, R. & McElrath, M. Antagonism of vaccine induced HIV-1 specific CD4 T cells by primary HIV-1 infection. Potential mechanism of vaccine failure. *J. Immunol.* **158,** 807–815 (1997).
28. Zinkernagel, R. M. Immunology taught by viruses. *Science* **271,** 173–178 (1996).
29. Bachmann, M. F., Speiser, D. & Ohashi, P. Functional Maturation of an antiviral CTL response. *J. Virol.* **71,** 5764–5768 (1997).
30. Battegay, M. *et al.* Quantification of LCMV with immunological focus assay in 24 or 96 well plates. *J. Virol. Meth.* **33,** 191–198 (1991).

Acknowledgements. This work was sponsored by the Wellcome Trust, the Swiss National Foundation for Science and the Kanton of Zurich. We thank E. Horvath for technical work, and P. Aichele, M. Bachmann, S. Ehl and A. McPherson for discussion.

Correspondence and requests for materials should be addressed to R.M.Z. (e-mail:rolf.zinkernagel@pty.unizh.ch).

Role of HIF-1α in hypoxia-mediated apoptosis, cell proliferation and tumour angiogenesis

Peter Carmeliet*, Yuval Dor†, Jean-Marc Herbert‡, Dai Fukumura§, Koen Brusselmans*, Mieke Dewerchin*, Michal Neeman‖, Françoise Bono‡, Rinat Abramovitch‖, Patrick Maxwell¶, Cameron J. Koch#, Peter Ratcliffe¶, Lieve Moons*, Rakesh K. Jain§, Désiré Collen* & Eli Keshet†

* *Center for Transgene Technology and Gene Therapy, Flanders Interuniversity Institute for Biotechnology, KU Leuven, Leuven B-3000, Belgium*
† *Department of Molecular Biology, Hebrew University-Hadassah Medical School, Jerusalem 91120, Israel*
‡ *Sanofi Recherche, Haemobiology Research Department, Toulouse Cedex 31036, France*
§ *Department of Radiation Oncology, Massachusetts General Hospital and Harvard Medical School, Boston, Massachussetts 02114, USA*
‖ *Department of Biological Regulation, Weizmann Institute of Science, Rehovot 76100, Israel*
¶ *Institute of Molecular Medicine, John Radcliffe Hospital, Wellcome Trust Centre for Human Genetics, Oxford OX3 7BN, UK*
# *Department of Radiation Oncology, School of Medicine, University of Pennsylvania, Philadelphia 19104-6003, USA*

As a result of deprivation of oxygen (hypoxia) and nutrients, the growth and viability of cells is reduced[1]. Hypoxia-inducible factor (HIF)-1α helps to restore oxygen homeostasis by inducing glycolysis, erythropoiesis and angiogenesis[2–4]. Here we show that hypoxia and hypoglycaemia reduce proliferation and increase apoptosis in wild-type (HIF-$1\alpha^{+/+}$) embryonic stem (ES) cells, but not in ES cells with inactivated HIF-1α genes (HIF-$1\alpha^{-/-}$); however, a deficiency of HIF-1α does not affect apoptosis induced by cytokines. We find that hypoxia/hypoglycaemia-regulated genes involved in controlling the cell cycle are either HIF-1α-dependent (those encoding the proteins p53, p21, Bcl-2) or HIF-1α-independent (p27, GADD153), suggesting that there are at

least two different adaptive responses to being deprived of oxygen and nutrients. Loss of HIF-1α reduces hypoxia-induced expression of vascular endothelial growth factor, prevents formation of large vessels in ES-derived tumours, and impairs vascular function, resulting in hypoxic microenvironments within the tumour mass. However, growth of HIF-1α tumours was not retarded but was accelerated, owing to decreased hypoxia-induced apoptosis and increased stress-induced proliferation. As hypoxic stress contributes to many (patho)biological disorders[1,5], this new role for HIF-1α in hypoxic control of cell growth and death may be of general pathophysiological importance.

HIF-1α$^{-/-}$ ES cells were generated by homologous recombination and subsequent selection in high G418 (Fig. 1a, b). ES clones harbouring a randomly integrated HIF-1α gene targeting vector

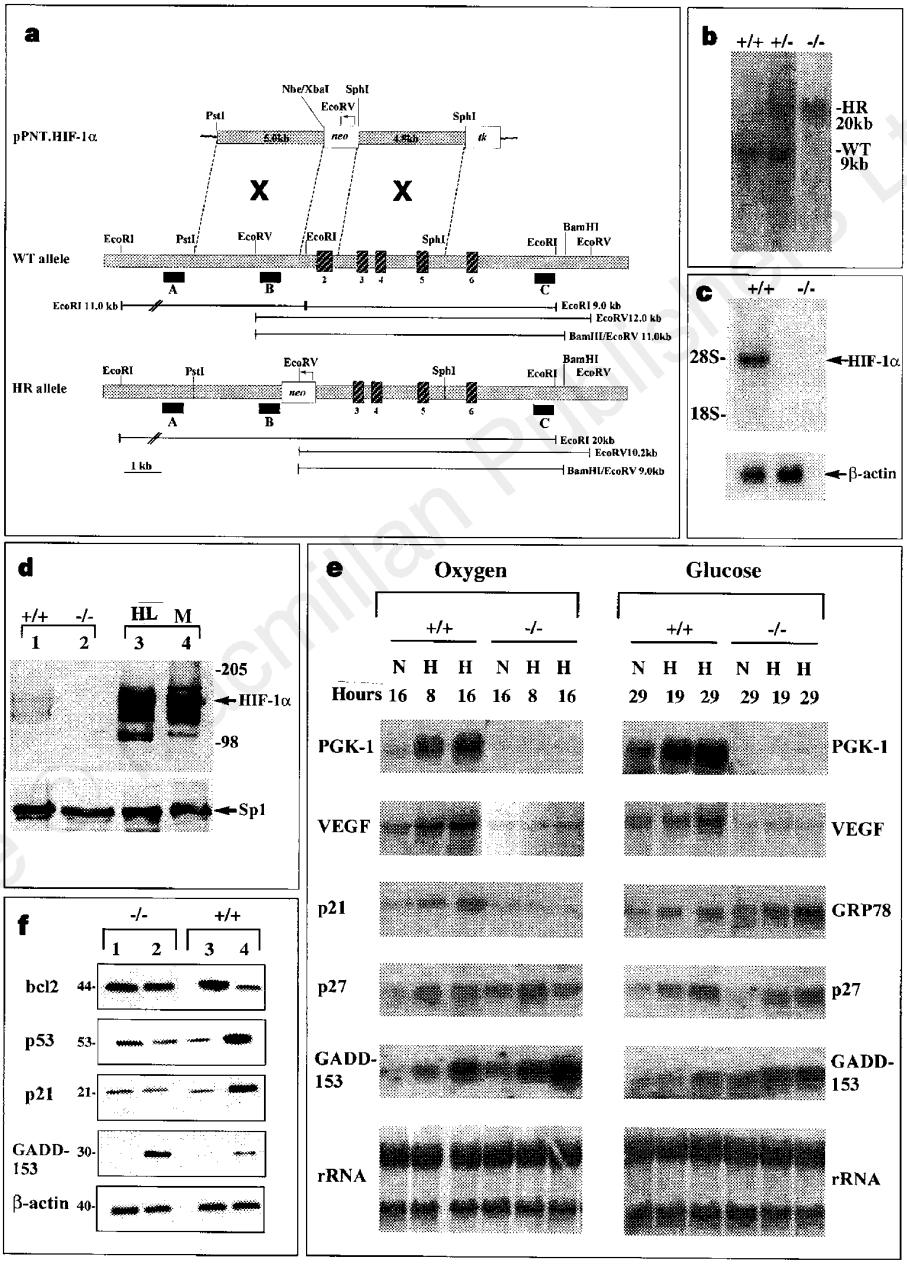

Figure 1 Targeting of the HIF-1α gene. **a**, Strategy to disrupt the HIF-1α gene. Top, targeting vector pPNT.HIF-1α; middle, map of the wild-type (WT) HIF-1α gene; bottom, homologously recombined (HR) *HIF-1α* allele with numbered exons (dark blocks) and introns (grey shaded bars). Hybridization probes A (0.5-kb *Hin*c2/*Pst*I fragment), B (1.5-kb *Stu*I/*Nhe*I fragment) and C (0.4-kb *Afl*2 fragment) and analytical restriction digests are indicated. **b**, Southern blot of *Eco*RI-digested genomic DNA from ES cell clones (probe C) generating a 9.0-kb WT and a 20.0-kb HR HIF-1α allele. **c**, Northern blot analysis of total mRNA from ES cells hybridized with a murine *HIF-1α* exon 2- specific cDNA probe or a β-actin probe. **d**, Western blot analysis for HIF-1α or the ubiquitous transcription factor Sp1 (control) on nuclear extracts from rHIF-1α$^{+/+}$ ES cells (lane 1), HIF-1α$^{-/-}$ ES cells (lane 2), human HeLa (HL) cells (lane 3) or mouse Hepa1 cells (M) (lane 4), treated with 100 μM desferrioxamine (DFO; 16 h). **e**, Northern blot analysis of total mRNA derived from undifferentiated rHIF-1α$^{+/+}$ (+/+) or HIF-1α$^{-/-}$ (–/–) ES cells during normoxia (N; 20% O_2) or hypoxia (H; 2% O_2), or during normoglycaemia (N; 25 mM glucose) or hypoglycaemia (H; 0 mM glucose) for the indicated time (hours). PGK-1, phosphoglycerokinase; VEGF: vascular endothelial growth factor; GADD153: growth arrest and DNA-damage-inducible gene 153; GRP78: glucose-regulated protein 78. The rRNA is shown as a control of loading. **f**, Western blot analysis on total cell extract from HIF-1α$^{-/-}$ (lanes 1, 2) or rHIF-1α$^{+/+}$ ES cells (lanes 3, 4) during normoxia (lanes 1, 3), during anoxia/hypoglycaemia (4 h; followed by recovery for 20 h in control conditions) for Bcl-2, p53, p21 (lanes 2, 4), or during hypoxia (2% O_2; 24 h) for GADD153 (lanes 2, 4); β-actin was used as control.

(rHIF-1α$^{+/+}$ cells) which survived high G418 selection were used as controls. Loss of HIF-1α gene function was confirmed by northern blotting (Fig. 1c), western blotting (Fig. 1d), and electrophoretic mobility shift assay (EMSA) (see also Fig. S1 in Supplementary Information, which is denoted by the prefix 'S'). Expression of known HIF-1α target genes (*VEGF*, *PGK-1*, *LDH-A*, *GLUT-1*)[3] was induced by hypoxia or hypoglycaemia in rHIF-1α$^{+/+}$ ES cells but barely occurred in HIF-1α$^{-/-}$ ES cells (Figs 1e and S2). Both HIF-1α-dependent (PGK-1 (ref. 3), VEGF (ref. 3), p21 (ref. 6)) and HIF-1α-independent (p27 (ref. 7), GADD153 (ref. 8), GRP78 (ref. 9)) regulation of target genes was observed, indicating that there must be at least two pathways for regulating hypoxic genes.

We studied hypoxia/hypoglycaemia-driven apoptosis by counting oligonucleosomes and cells labelled with terminal deoxytransferase-mediated deoxyuridine nick end-labelling (TUNEL). Apoptosis was comparable in rHIF-1α$^{+/+}$ and HIF-1α$^{-/-}$ ES cells during normoxia/normoglycaemia and increased to a similar extent after stimulation with a cytokine mixture (Table 1). In contrast, during normoglycaemia/hypoxia, hypoglycaemia/normoxia, normoxia in the presence of 2-deoxyglucose, or hypoglycaemia/anoxia, apoptosis increased 10–30-fold in rHIF-1α$^{+/+}$ ES cells but was unaffected in HIF-1α$^{-/-}$ ES cells (Table 1). Hypoxia also induced apoptosis in wild-type C4.5 cells[10] but not in HIF-1α-deficient Ka13 Chinese hamster ovary (CHO) cells[10] (Table S1), indicating that HIF-1α could be a general mediator of hypoxia/hypoglycaemia-driven apoptosis. The levels of p53 (a mediator of a genotoxic apoptosis[11,12] that is upregulated during hypoxia[13]) and of p21 (a p53 target gene and effector of cell-cycle arrest[6]) were significantly increased, whereas the amount of the apoptosis-inhibitor Bcl-2 (ref. 14) was reduced in stressed rHIF-1α$^{+/+}$ but not in HIF-1α$^{-/-}$ ES cells (Fig. 1e, f and Table 1). Conversely, hypoxia-induced levels of the pro-apoptotic and growth-arrest gene product GADD153 (ref. 8) and of the cyclin-dependent kinase inhibitor p27 (ref. 7) occurred independently of HIF-1α (Fig. 1e, f).

Hypoxic stress suppressed proliferation of rHIF-1α$^{+/+}$ ES cells, cultured either as undifferentiated monolayers or as differentiated three-dimensional embryoid bodies (Table 1). In contrast, it did not alter proliferation of HIF-1α$^{-/-}$ ES cell monolayers, but significantly increased proliferation in HIF-1α$^{-/-}$ embryoid bodies (Table 1). Thus, HIF-1α deficiency prevents cells from undergoing hypoxic growth arrest and, in the appropriate (mitogenic) microenvironment, stimulates proliferation. In previous studies, loss of HIF-1α[4,15] or of its heterodimer HIF-1β/ARNT[16] did not significantly alter or reduce the accumulation of cells during hypoxia or hypoglycaemia, although proliferation and apoptosis were not measured directly. Whether, and to what extent, the role of HIF-1α and of HIF-1β in cell proliferation and apoptosis depends on genotype, cell type or experimental conditions such as pH[17], cell density,

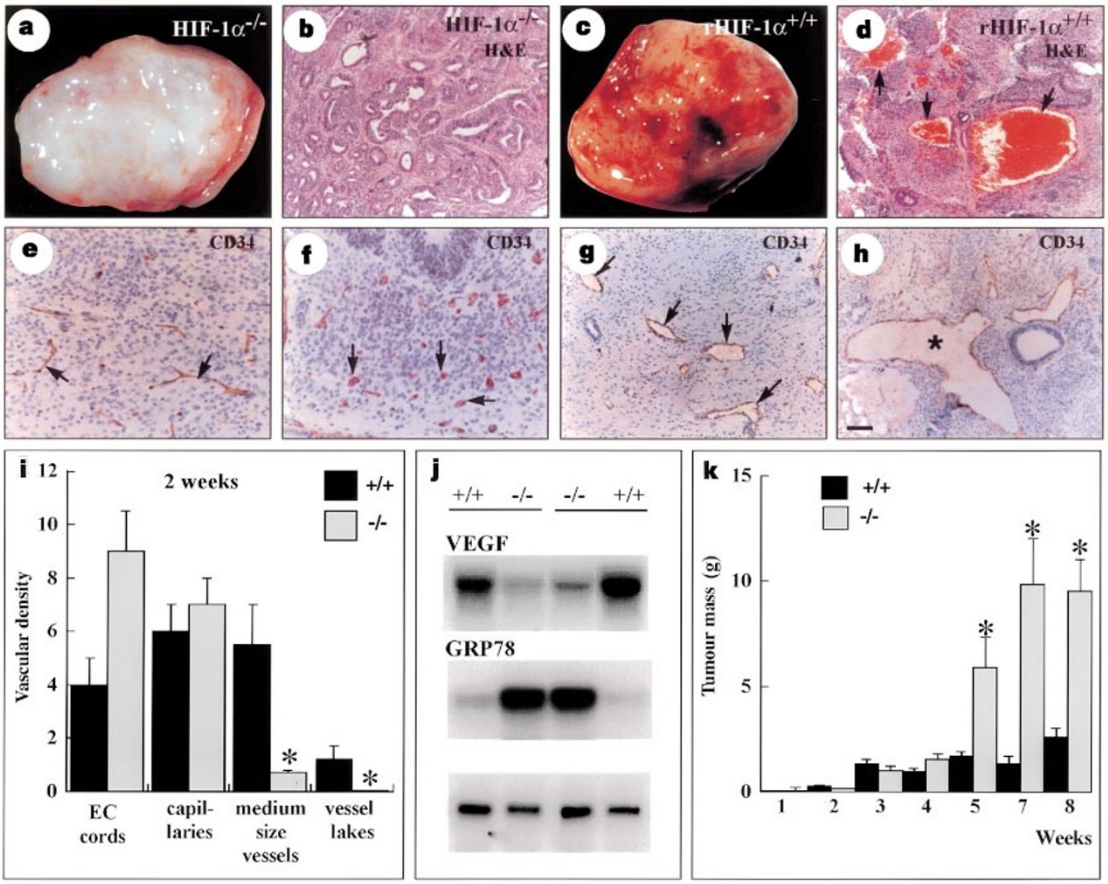

Figure 2 Vascularization of HIF-1α$^{-/-}$ and rHIF-1α$^{+/+}$ tumours. **a**–**d**, Macroscopic (**a**, **c**) and haematoxylin–eosin stained (**b**, **d**) sections through HIF-1α$^{-/-}$ (**a**, **b**) and rHIF-1α$^{+/+}$ (**c**, **d**) tumours revealing the red/haemorrhagic phenotype in rHIF-1α$^{+/+}$ tumours which contrast to the white and poorly vascularized HIF-1α$^{-/-}$ tumours. Note the large blood vessels in **d** (arrows) and their absence in **b**. The blood around the HIF-1α$^{-/-}$ tumour (**a**) has leaked from blood vessels in its surrounding capsule. **e**–**h**, CD34-immunostained sections through HIF-1α$^{-/-}$ (**e**, **f**) and rHIF-1α$^{+/+}$ (**g**, **h**) tumours revealing the presence of endothelial cords (<2 μm; arrows in **e**) and capillaries (~8 μm; arrows in **f**) in HIF-1α$^{-/-}$ tumours, and the presence of medium-sized vessels (~30 × 70 μm; arrows in **g**) and large blood vessel lakes ~90 × 280 μm; asterisk in **h**) in the rHIF-1α$^{+/+}$ tumours. **i**, Vascular density (mean ± s.e.m.) of the different types of blood vessels per optical field in 7 or 8 two-week-old tumours. Asterisks, $P < 0.05$ versus rHIF-1α$^{+/+}$ by unpaired Student's *t*-test. Similar data were obtained at 4 and 7 weeks (Table S2). **j**, Northern blot analysis from rHIF-1α$^{+/+}$ and HIF-1α$^{-/-}$ tumours for VEGF, GRP78 and β-actin (control). **k**, Growth rate of HIF-1α$^{-/-}$ (shaded bars) and rHIF-1α$^{+/+}$ (black bars) tumours. Asterisks, $P < 0.05$ versus rHIF-1α$^{+/+}$. The bar in **h** represents 50 μm in **e**, **f**; 100 μm in **g**, **h**; 200 μm in **b**, **d**; and 25 mm in **a**, **c**.

Table 1 Apoptosis and proliferation in HIF-1$\alpha^{-/-}$ and rHIF-1$\alpha^{+/+}$ ES cells

			Normoxia/ normoglycaemia	Hypoxia/ normoglycaemia	Normoxia/ hypoglycaemia	Normoxia/ 2-deoxyglucose	Anoxia/ hypoglycaemia
Apoptosis	Oligonucleosomes	rHIF-1$\alpha^{+/+}$	32 ± 5	370 ± 20*	130 ± 11*	130 ± 12*	1,300 ± 120*
		+ cytokines	360 ± 12*	ND	ND	ND	ND
		HIF-1$\alpha^{-/-}$	34 ± 3	31 ± 2	41 ± 1	37 ± 4	45 ± 6
		+ cytokines	380 ± 20*	ND	ND	ND	ND
	TUNEL-positive cells	rHIF-1$\alpha^{+/+}$	4.3 ± 0.19	36 ± 2*	26 ± 1.8*	23 ± 2*	61 ± 4*
		HIF-1$\alpha^{-/-}$	3.7 ± 0.12	4.5 ± 0.2	7.2 ± 1.7	5 ± 1	7 ± 2
	Bcl-2	rHIF-1$\alpha^{+/+}$	100 ± 12	27 ± 4*	31 ± 4*	45 ± 1.9*	11 ± 1*
		HIF-1$\alpha^{-/-}$	110 ± 9	120 ± 12	96 ± 9	120 ± 7.3	110 ± 16
	p21	rHIF-1$\alpha^{+/+}$	0.41 ± 0.1	1.2 ± 0.2*	0.93 ± 0.1*	0.74 ± 0.2*	1.5 ± 0.2*
		HIF-1$\alpha^{-/-}$	0.34 ± 0.1	0.33 ± 0.1	0.32 ± 0.1	0.37 ± 0.1	0.3 ± 0.1
	p53	rHIF-1$\alpha^{+/+}$	0.11 ± 0.03	3.1 ± 0.1*	2.4 ± 0.1*	2.2 ± 0.04*	3.9 ± 0.13*
		HIF-1$\alpha^{-/-}$	0.12 ± 0.04	0.13 ± 0.04	0.11 ± 0.07	0.10 ± 0.03	0.14 ± 0.13
Proliferation	c.p.m. ^{3}H-thymidine	rHIF-1$\alpha^{+/+}$	3,500 ± 400	2,500 ± 300*	ND	ND	ND
		HIF-1$\alpha^{-/-}$	3,600 ± 470	3,400 ± 380	ND	ND	ND
	BrdU-positive cell fraction	rHIF-1$\alpha^{+/+}$	24 ± 4	5 ± 1*	ND	ND	9 ± 2*
		HIF-1$\alpha^{-/-}$	23 ± 5	46 ± 8*	ND	ND	50 ± 10*

The data represent the mean ± s.d. (n is 9 to 12) of the number of oligonucleosomes, the units of Bcl-2 and p21, or the pg amounts of p53 antigen, all per 10^5 cells; or the mean ± s.e.m. (n, 8–10) of the fraction of TUNEL- or BrdU-positive cells (per cent of total), or the amount of c.p.m. ^{3}H-thymidine incorporated per 24 well. ND, not done.
* Statistical significance ($P < 0.05$) versus control (normoxia/normoglycaemia without cytokines) by unpaired Student's t-test.

oxygen or glucose concentrations, or the amount of serum or growth factors (unpublished observations), some of which regulate apoptosis induced by other types of stress[12,18,19] is still unclear.

To extend our *in vitro* data, rHIF-1$\alpha^{+/+}$ and HIF-1$\alpha^{-/-}$ ES cells were subcutaneously injected into nude mice. HIF-1$\alpha^{-/-}$ tumours (44 analysed) were most often (75%) homogeneously white, with minimal bleeding (Fig. 2a), and less frequently (25%) slightly haemorrhagic. In contrast, rHIF-1$\alpha^{+/+}$ tumours (33 analysed) usually (82%) bled profusely and severely, with fewer tumours (18%) being mildly haemorrhagic (Fig. 2c). HIF-1$\alpha^{-/-}$ tumours lacked medium-sized and large vessels but not endothelial cords or capillaries (Fig. 2b, d, e–i; Table S2). Magnetic resonance imaging (MRI) and intravital microscopy (Fig. 3a–d) revealed that HIF-1$\alpha^{-/-}$ tumours had a uniform vascularization pattern, with fewer large blood vessels and more avascular zones than rHIF-1$\alpha^{+/+}$ tumours, which were characterized by a variable and irregular vascular network, typical of many tumours[20]. The intravital haemodynamics in rHIF-1$\alpha^{+/+}$ tumours compared with HIF-1$\alpha^{-/-}$ tumours were (mean ± s.e.m.): vessel density (total length of vessels per unit area in $\mathrm{cm\,cm^{-2}}$), 120 ± 16 ($n = 18$) versus 86 ± 14 ($n = 25$; $P < 0.05$ by ANOVA); vessel diameter (μm), 21 ± 2 ($n = 16$) versus 14 ± 1 ($n = 21$; $P < 0.05$); and flow rate (picolitre $\mathrm{s^{-1}}$): 220 ± 50 ($n = 44$) versus 90 ± 13 ($n = 44$; $P < 0.05$). This vascular phenotype may be due to a lack of upregulation of the expression of vascular endothelial growth factor (VEGF) in hypoxic areas of HIF-1$\alpha^{-/-}$ tumours (Figs 2j and S3a, c, g)[21].

Injection of microspheres revealed a lower blood flow through HIF-1$\alpha^{-/-}$ than through rHIF-1$\alpha^{+/+}$ tumours ($0.079 \pm 0.0027\ \mathrm{ml\,min^{-1}\,g^{-1}}$ versus $0.16 \pm 0.046\ \mathrm{ml\,min^{-1}\,g^{-1}}$; $n = 6$; $P = 0.013$ by paired Student's t-test). MRI analysis was used to measure blood flow and changes in oxygenated haemoglobin in response to changes in inspired oxygen. Perfusion and oxygenation were lower in HIF-1$\alpha^{-/-}$ than in rHIF-1$\alpha^{+/+}$ tumours, as evidenced by the 10-fold lower $b\Delta Y$ values (where b is ml blood per ml tissue and ΔY is the change in oxyhaemoglobin fraction/total haemoglobin; see Methods) (Fig. 3a, b): the mean enhancement of $b\Delta Y$ (a parameter of general O_2 delivery) was 0.014 ± 0.002 in rHIF-1$\alpha^{+/+}$ tumours versus 0.0016 ± 0.0008 in HIF-1$\alpha^{-/-}$ tumours ($n = 4$; $P < 0.001$ by t-test; Table S3). Optical measurement of the pO_2 revealed consistently lower values in HIF-1$\alpha^{-/-}$ than in rHIF-1$\alpha^{+/+}$ tumours (Fig. 3e). HIF-1$\alpha^{-/-}$ tumours also had 3-fold more hypoxic areas than did rHIF-1$\alpha^{+/+}$ tumours (Fig. 3f, g), as revealed by staining for the hypoxia marker EF5 (fractional EF5-positive area: 3.6 ± 0.7% versus 1.1 ± 0.4%, respectively; $n = 11$; $P < 0.005$). Whereas levels of the HIF-1α target gene encoding VEGF (frequently co-expressed with GRP78 in microenvironments close to necrosis; Fig. 2j and Fig. S3a–d) were higher in rHIF-1$\alpha^{+/+}$ than in HIF-1$\alpha^{-/-}$ tumours, expression of the HIF-1α-independent stress-induced marker GRP78 (and GADD153; not shown) was stronger and more widespread in HIF-1$\alpha^{-/-}$ than in rHIF-1$\alpha^{+/+}$ tumours (Figs 2j and S3b, g, h), indicating that hypoxic/hypoglycaemic stress was greater in HIF-1$\alpha^{-/-}$ than in rHIF-1$\alpha^{+/+}$ tumours.

Although the diminished vascular supply would be expected to reduce the rate of HIF-1$\alpha^{-/-}$ tumour growth, growth rates were comparable during the first 3 weeks, being similar to what has been observed for ARNT$^{-/-}$ ES cell tumour growth (C. Simon, personal communication), but then growth of HIF-1$\alpha^{-/-}$ tumours far exceeded that of rHIF-1$\alpha^{+/+}$ tumours (Fig. 2k). Cellular proliferation (measured as the percentage of PCNA-positive cells, where PCNA is proliferating cell nuclear antigen) was comparable in 2-week-old tumours (4.7 ± 2.3% in rHIF-1$\alpha^{+/+}$ versus 8.1 ± 2.3% in HIF-1$\alpha^{-/-}$ tumours; P = NS), but at 4 to 7 weeks was significantly higher in HIF-1$\alpha^{-/-}$ tumours (11 ± 2% and 18 ± 2%, respectively) than in rHIF-1$\alpha^{+/+}$ tumours (3.4 ± 1.6% and 3.4 ± 1.0%; $P < 0.05$). In rHIF-1$\alpha^{+/+}$ tumours, cell proliferation in 134 EF5-positive hypoxic fields was absent (in 49%) or minimal (in 51%) (as indicated by the few PCNA-positive cells in a stressed GRP78-positive rHIF-1$\alpha^{+/+}$ field; Fig. S3e). In contrast, in HIF-1$\alpha^{-/-}$ tumours, hypoxia appeared directly to stimulate proliferation, as 75% of 157 EF5-positive fields were intensely labelled for PCNA (as shown by the many PCNA-labelled cells within a stressed GRP78-positive HIF-1$\alpha^{-/-}$ field in Fig. S3i). Thus, similar genotypic differences in hypoxic control of proliferation were observed in tumours and in embryoid bodies. In addition, loss of HIF-1α affected tumour growth by progressive selection of intensely proliferating cells, as occurs in the absence of p53 (ref. 22). Indeed, PCNA-labelled cells (predominantly epitheloid cells) accumulated more in HIF-1$\alpha^{-/-}$ tumours than in rHIF-1$\alpha^{+/+}$ tumours (fractional epitheloid area: 26 ± 8%, 46 ± 4%, 46 ± 3% in HIF-1$\alpha^{-/-}$ tumours, and 37 ± 6%, 18 ± 3%, 9 ± 2% in rHIF-1$\alpha^{+/+}$ tumours at 2, 4 and 7 weeks, respectively; $P < 0.05$ versus HIF-1$\alpha^{-/-}$ at 4 and at 7 weeks; Fig. S3m, n).

Apoptosis (quantified by the number of oligonucleosomes per mg protein) was consistently lower in HIF-1$\alpha^{-/-}$ tumours

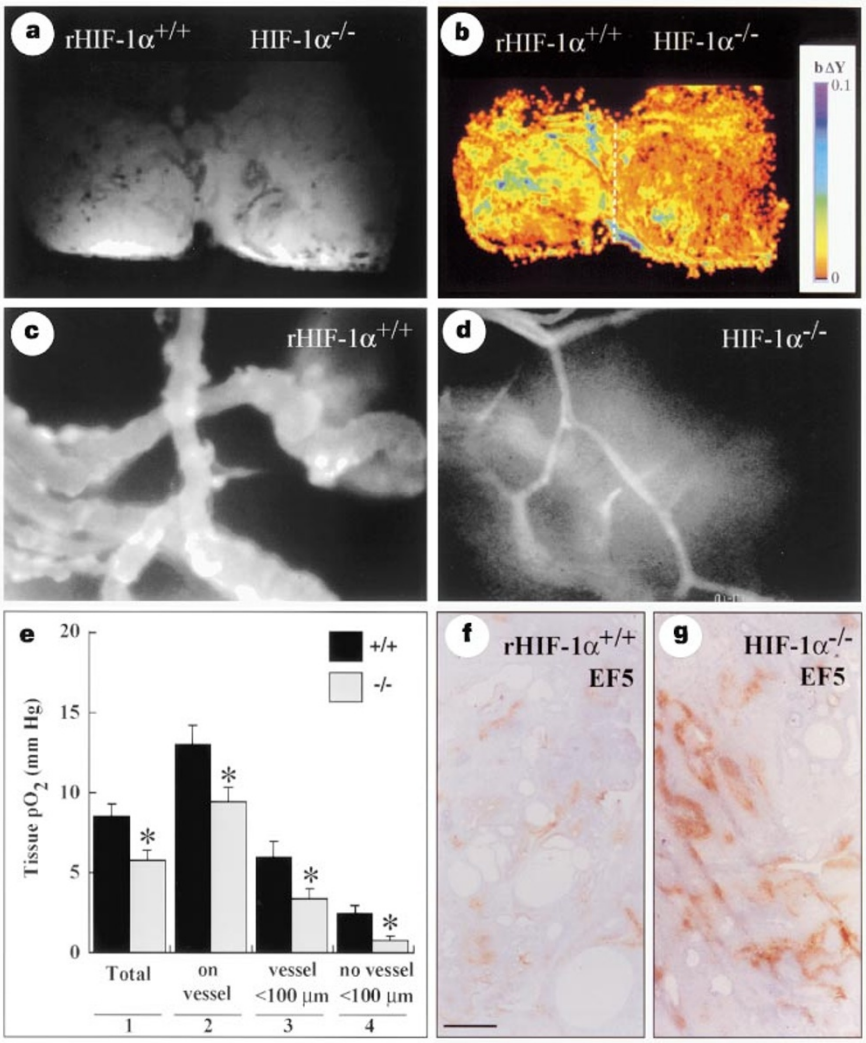

Figure 3 Functional vascularization and growth of HIF-1$\alpha^{-/-}$ and rHIF-1$\alpha^{+/+}$ tumours. **a**, **b**, Gradient echo magnetic resonance imaging (MRI) of a rHIF-1$\alpha^{+/+}$ (left) and HIF-1$\alpha^{-/-}$ (right) tumour during inhalation of 95% oxygen and 5% CO_2. **a**, Greyscale original MRI image; **b**, calculated 'functional vascular' ($b\Delta Y$) map of the same tumours. Colour code of $b\Delta Y$: minimum '0' (red) indicates undetectable oxygen delivery; maximum '0.1' (purple) reflects the degree of oxygen delivery in a large perfused vessel. For details, see Methods. The HIF-1$\alpha^{-/-}$ and rHIF-1$\alpha^{+/+}$ tumours were mounted so that their overlying skin appears merged on the image (white dotted line). **c**, **d**, FITC fluorescence images of microvessels in a rHIF-1$\alpha^{+/+}$ (**c**) and HIF-1$\alpha^{-/-}$ (**d**) tumour by intravital fluorescence microscopy after intravenous injection of FITC–dextran. **e**, Tissue pO_2 values (mean ± s.e.m.) in rHIF-1$\alpha^{+/+}$ and HIF-1$\alpha^{-/-}$ tumours. (1) 'Total': average pO_2 throughout the entire tumour; (2) 'on vessel': blood vessel within high-resolution tissue pO_2 sampling field (40 μm in diameter); (3) 'vessel < 100 μm': blood vessels within 100 μm from tissue pO_2 sampling field; (4) 'no vessel < 100 μm': no blood vessel within 100 μm from tissue pO_2 sampling field. Asterisks, $P < 0.05$ versus rHIF-1$\alpha^{+/+}$ by unpaired *t*-test. **f**, **g**, EF5 staining of a rHIF-1$\alpha^{+/+}$ (**f**) and HIF-1$\alpha^{-/-}$ (**g**) tumour, revealing more, and more strongly, stained hypoxic areas in the HIF-1$\alpha^{-/-}$ tumour. Scale bar, 200 μm in **f**, **g**; 100 pixels in **c**, **d** represent 100 μm; tumours in **a**, **b** weighed ~3 g each.

(870 ± 50, 1,600 ± 100 and 2,500 ± 150 at 2, 4 and 7 weeks) than in rHIF-1$\alpha^{+/+}$ tumours (1,500 ± 130, 2,200 ± 200 and 3,100 ± 100 at 2, 4 and 7 weeks: $P < 0.05$). Most (85%) TUNEL-positive fields were also EF5-positive in tumours of both genotypes (Fig. S3k, l), confirming that apoptosis *in vivo* is hypoxia-driven. Whereas tumours of both genotypes had comparable TUNEL/EF5-positive fields (74% of 134 EF5-positive fields in rHIF-1$\alpha^{+/+}$ tumours, 80% of 160 EF5-positive zones in HIF-1$\alpha^{-/-}$ tumours), fewer apoptotic cells were present in HIF-1$\alpha^{-/-}$ tumour fields (2.5 ± 0.2% versus 1.5 ± 0.2% cross-sectional area; $P < 0.05$; Fig. S3f, j). The less obvious hypoxic apoptosis *in vivo* than *in vitro* may relate to differences in environmental signals, influencing the switch towards growth arrest and survival rather than apoptosis, as shown for apoptosis induced by other types of stress[12,18].

Many tumours contain hypoxic microenvironments, a condition that is associated with poor prognosis and resistance to treatment[20,23]. Our findings indicate that tumour vascularization is largely controlled by HIF-1α, in part as a result of upregulation of VEGF. In addition, a new role for HIF-1α in hypoxic control of growth and apoptosis has been revealed, the *in vivo* significance of which is indicated by the genotype-dependent differences in tumour growth. The HIF-1α-dependent growth arrest/apoptosis in response to hypoxia is reminiscent of the p53-mediated control of growth arrest/apoptosis in response to genotoxic or physical stresses[11,12]. Furthermore, the HIF-1α-dependent induction of p53, p21 and suppression of Bcl-2 during hypoxic growth arrest/apoptosis may reflect an interplay between these pathways. Indeed, hypoxia can stabilize p53 by binding HIF-1α (ref. 24). The effects of losing HIF-1α on the cell's behaviour confirm the importance of this molecular interaction. As HIF-1α is activated in solid tumours, our results suggest a new general mechanism for tumour growth. □

Methods

HIF-1α targeting, ES cells, embryoid bodies and tumour formation. The HIF-1α targeting vector (pPNT.HIF-1α; Fig. 1a) contained a 5′ flanking 5.0-kb *Pst*I/*Nhe*I fragment upstream of exon 2, and a 3′ flanking 4.8-kb *Sph*I fragment downstream of exon 2. Culture and targeting of undifferentiated ES cells, including selection in high G418, northern blot and western blot analysis, and EMSA were done as described[25,26]. For mRNA studies, ES cells were weaned off fibroblast feeders in the presence of leukaemia-inhibitory factor (LIF; ESGRO, GIBCO-BRL and Life Technologies). Cells at 75% confluency were cultured in normoxia (20% O_2)/normoglycaemia (25 mM glucose), in anoxia (<0.1% O_2; 6 h; BBL Gaspack 100 Anaerobic system, Beckton Dickinson), in hypoxia (0.5 or 2% O_2; 8–16 h) or in glucose-free medium (19 or 29 h) before mRNA analysis. Embryoid bodies (EBs) were generated by culturing ES cells (without feeders) in hanging drops (300 cells per 30 μl) in medium without LIF for 3 d, and then on bacterial dishes for 2–8 weeks. EBs (3 weeks for *in situ* hybridization, 6 to 8 weeks for proliferation analysis) were stressed in hypoxia (1% O_2 for 24 h), or in glucose-free medium/anoxia (4 h; followed by 20 h recovery in normoxia/normoglycaemia). For ES-cell-derived tumour formation, 5×10^6 ES cells were subcutaneously injected into *Nu/Nu* mice.

Intravital microscopy, magnetic resonance imaging and flow. All methods for intravital microscopy of ES-cell-derived tumours in dorsal skin chambers, implanted in *Nu/Nu* mice including measurements of the velocity of red blood cells (V_{RBC}), blood-flow rates, vessel diameter and vessel density (defined as the total length of vessels per unit area; cm cm^{-2}), and tissue pO_2 measurements were made at 15 to 17 days on tumours 8 to 10 mm in diameter (0.3 g) as described[23]. Gradient echo MRI has been described[27]. Vascular functionality ($b\Delta Y$) maps were derived from the average images, obtained by inhaling carbogen (95% O_2–5% CO_2) or air–CO_2 (95% air–5% CO_2); $b\Delta Y = (I_{carbon}/I_{air--CO_2})/TE \times C_{MRI}$, where '$b$' is the volume fraction of blood, ΔY is the change in fraction of oxyhaemoglobin, TE is time to echo (10 ms) and $C_{MRI} = 599\,s^{-1}$ at 4.7 T. Blood flow in tumours was measured using 15-μm coloured microspheres as described[28].

Histology, immunostaining and *in situ* hybridization. All methods for histology, immunostaining, and *in situ* hybridization have been described[26,29]. Vascular densities were quantified by counting the number of endothelial cords (consisting of two closely apposed endothelial cell layers without detectable lumen; <2 μm wide; Fig. 2e), capillaries with a small lumen (diameter 7 ± 5 μm; Fig. 2f), medium-sized vessels with a larger lumen (30 ± 3 μm versus 70 ± 5 μm for medium and large diameter, respectively; Fig. 2g), or blood vessel lakes with the largest lumen (90 ± 14 μm, short axis versus 280 ± 50 μm, long axis; Fig. 2h) per field (1.2 mm^2) in 6 to 8 randomly chosen optical fields on 3 to 5 adjacent sections (320 μm apart) per tumour. The fractional area of epitheloid cells (identified morphologically by their typical histological appearance and high cell density; Fig. S3n inset) was morphometrically quantified using the Quantimed Q600 imaging system.

Apoptosis and proliferation. For apoptosis studies, undifferentiated ES monolayers were cultured at 10,000 cells in 24-well dishes in normal ES cell medium containing 5% fetal calf serum for 24 h, and stressed for 24 h in the same medium without LIF under hypoxic or hypoglycaemic conditions. Apoptosis was measured using an ELISA (Boehringer Mannheim) for cytoplasmic histone-associated DNA fragments (mono- and oligonucleosomes), expressed as the number of oligonucleosomes per 10^5 cells (undifferentiated ES cells) or per mg protein (tumours)[30]. TUNEL-positive cells were visualized using an ApopTag kit (Oncor). Interleukin-1β (3 ng ml^{-1}), interferon-γ (5 ng ml^{-1}), and tumour-necrosis factor-α (30 ng ml^{-1}) (all from R & D Systems) were added during normoxia/normoglycaemia for 24 h to induce hypoxia/hypoglycaemia-independent apoptosis. Oligonucleosomes (number per 10^5 cells) and antigen levels of Bcl-2 (units per 10^5 cells), p21 (units per 10^5 cells) and p53 (pg per 10^5 cells) were quantified by ELISA (Calbiochem). Apoptosis in hypoxic tumour zones was morphometrically quantified using the Quantimed Q600 imaging system by measuring the area of TUNEL-immunoreactive cells per hypoxic zone. Between 8 and 10 randomly chosen zones on 8 to 10 sections (320 μm apart) were analysed and averaged per tumour. Western blotting of cell-cycle-control genes was done on whole-cell extracts using antibodies specific against p53, p21, Bcl-2 (all from Calbiochem), GADD153 (Santa Cruz Biotechnology) or β-actin (Sigma).

For analysis of proliferation of undifferentiated ES cell monolayers, ES cells (plated at 7,000 cells in 24-well dishes and serum-starved for 24 h) were stressed for 24 h in hypoxia (2% O_2; 24 h), incubated with 1 μCi ^{3}H-thymidine for 2 h, and the incorporated ^{3}H-thymidine counted[30]. For analysis of proliferation in EBs, 6–8-week-old EBs were stressed under hypoxia (1% O_2, 24 h), or under hypoglycaemia/anoxia for 4 h, followed by a 20-h recovery in normoxia/normoglycaemia, in medium containing 5′-bromo-2′,3′-deoxyuridine (BrdU; 30 μM). *In situ* morphometric analysis of proliferation was done by measuring the area of all PCNA-immunoreactive cells on cross-section through each tumour (~150 mm^2) and expressing it as a percentage of the tumour area analysed.

Received 2 April; accepted 12 June 1998.

1. Bunn, H. F. & Poyton, R. O. Oxygen sensing and molecular adaptation to hypoxia. *Physiol. Rev.* **76,** 839–885 (1996).
2. Wenger, R. H. & Gassmann, M. Oxygen(s) and the hypoxia-inducible factor-1. *Biol. Chem.* **378,** 609–616 (1997).
3. Semenza, G. L. Transcriptional regulation by hypoxia-inducible factor-1. *Trends Cardiovasc. Med.* **6,** 151–157 (1996).
4. Iyer, N. V. *et al.* Cellular and developmental control of O_2 homeostasis by hypoxia-inducible factor-1α. *Genes Dev.* **12,** 149–162 (1998).
5. Dor, Y. & Keshet, E. Ischemia-driven angiogenesis. *Trends Cardiovasc. Med.* **7,** 289–294 (1997).
6. Gartel, A. L., Serfas, M. S. & Tyner, A. L. p21–negative regulator of the cell cycle. *Proc. Soc. Exp. Biol. Med.* **213,** 138–149 (1996).
7. Toyoshima, H. & Hunter, T. p27, a novel inhibitor of G1 cyclin-Cdk protein kinase activity, is related to p21. *Cell* **78,** 67–74 (1994).
8. Price, B. D. & Calderwood, S. K. Gadd45 and Gadd153 messenger RNA levels are increased during hypoxia and after exposure of cells to agents which elevate the levels of the glucose-regulated proteins. *Cancer Res.* **52,** 3814–3817 (1992).
9. Little, E., Ramakrishnan, M., Roy, B., Gazit, G. & Lee, A. S. The glucose-regulated proteins (GRP78 and GRP94): functions, gene regulation, and applications. *Crit. Rev. Eukaryot. Gene Expr.* **4,** 1–18 (1994).
10. Wood, S. M. *et al.* Selection and analysis of a mutant cell line defective in the hypoxia-inducible factor-1α subunit. Characterization of HIF-1α dependent and independent hypoxia-inducible gene expression. *J. Biol. Chem.* **273,** 8360–8367 (1998).
11. Liebermann, D. A., Hoffman, B. & Steinman, R. A. Molecular controls of growth arrest and apoptosis: p53-dependent and independent pathways. *Oncogene* **11,** 199–210 (1995).
12. Cox, L. S. Multiple pathways control cell growth and transformation: overlapping and independent activities of p53 and p21Cip1/WAF1/Sdi1. *J. Pathol.* **183,** 134–140 (1997).
13. Graeber, T. G. *et al.* Hypoxia induces accumulation of p53 protein, but activation of a G1-phase checkpoint by low-oxygen conditions is independent of p53 status. *Mol. Cell. Biol.* **14,** 6264–6277 (1994).
14. Strasser, A., Huang, D. C. & Vaux, D. L. The role of the bcl-2/ced-9 gene family in cancer and general implications of defects in cell death control for tumorigenesis and resistance to chemotherapy. *Biochim. Biophys. Acta* **1333,** F151–178 (1997).
15. Maxwell, P. H. *et al.* Hypoxia-inducible factor-1 modulates gene expression in solid tumors and influences both angiogenesis and tumor growth. *Proc. Natl Acad. Sci. USA* **94,** 8104–8109 (1997).
16. Maltepe, E., Schmidt, J. V., Baunoch, D., Bradfield, C. A. & Simon, C. M. Abnormal angiogenesis and responses to glucose and oxygen deprivation in mice lacking the protein ARNT. *Nature* **386,** 403–407 (1997).
17. Schmaltz, C., Harrigan Hardenbergh, P., Wells, A. & Fisher, D. E. Regulation of proliferation–survival decisions during tumor cell hypoxia. *Mol. Cell. Biol.* **18,** 2845–2854 (1998).
18. Collins, M. K., Perkins, G. R., Rodriguez Tarduchy, G., Nieto, M. A. & Lopez Rivas, A. Growth factors as survival factors: regulation of apoptosis. *Bioessays* **16,** 133–138 (1994).
19. Lin, Y. & Benchimol, S. Cytokines inhibit p53-mediated apoptosis but not p53-mediated G1 arrest. *Mol. Cell. Biol.* **15,** 6045–6054 (1995).
20. Vaupel, P. The influence of tumor blood flow and microenvironmental factors on the efficacy of radiation, drugs and localized hyperthermia. *Klin. Pädiatr.* **209,** 243–249 (1997).
21. Yuan, F. *et al.* Time-dependent vascular regression and permeability changes in established human tumor xenografts induced by an anti-vascular endothelial growth factor/vascular permeability factor antibody. *Proc. Natl Acad. Sci. USA* **93,** 14765–14770 (1996).
22. Graeber, T. G. *et al.* Hypoxia-mediated selection of cells with diminished apoptotic potential in solid tumours. *Nature* **379,** 88–91 (1996).
23. Helmlinger, G., Yuan, F., Dellian, M. & Jain, R. K. Interstitial pH and pO_2 gradients in solid tumors *in vivo*: high-resolution measurements reveal a lack of correlation. *Nature Med.* **3,** 177–182 (1997).
24. An, W. G. *et al.* Stabilization of wild-type p53 by hypoxia-inducible factor-1α. *Nature* **392,** 405–408 (1998).
25. Jiang, B. H., Rue, E., Wang, G. L., Roe, R. & Semenza, G. L. Dimerization, DNA binding, and transactivation properties of hypoxia-inducible factor-1. *J. Biol. Chem.* **271,** 17771–17778 (1996).
26. Carmeliet, P. *et al.* Abnormal blood vessel development and lethality in embryos lacking a single vascular endothelial growth-factor allele. *Nature* **380,** 435–439 (1996).
27. Abramovitch, R., Frenkiel, D. & Neeman, M. Analysis of subcutaneous angiogenesis by gradient echo magnetic resonance imaging. *Magn. Reson. Med.* **39,** 813–824 (1998).
28. Kobayashi, N., Kobayashi, K., Kouno, K., Horinaka, S. & Yagi, S. Effects of intra-arterial injection of colored microspheres on systemic hemodynamics and regional blood flow in rats. *Am. J. Physiol.* **266,** H1910–H1917 (1994).
29. Evans, S. M. *et al.* Identification of hypoxia in cells and tissues of epigastric 9L rat glioma using EF5 (2-(2-nitro-1H-imidazol-1-yl)-*N*-(2,2,3,3,3-pentafluoropropyl) acetamide). *Br. J. Cancer* **72,** 875–882 (1995).
30. Herbert, J. M. & Carmeliet, P. Involvement of u-PA in the anti-apoptotic activity of TGFβ for vascular smooth muscle cells. *FEBS Lett.* **413,** 401–404 (1997).

Supplementary information is available on *Nature*'s World-Wide Web site (http://www.nature.com) or as paper copy from the London editorial office of *Nature*.

Acknowledgements. We thank D. Livingston for monoclonal HIF-1α antibodies; M. Lampugnani and E. Dejana for CD31 antibodies; E. M. Lord for ALK3.51 antibodies; G. Suske for Sp1 antibodies; S. Plaisance and G. Theilmeier for discussion and for their help; K. Bijnens, A. Bouché, I. Cornelissen, M. De Mol, E. Gils, B. Hermans, S. Jansen, L. Kieckens, A. Manderveld, T. Vancoetsem, A. Vandenhoeck, A. Van den Boomen, P. Van Wesemael, S. Wyns (Leuven), A. Itin, I. Lamarche, P. Rogon, Y. Chen, J. Kahn and T. Gohongi for technical assistance; and M. Deprez for artwork. This work was supported in part by a NCI-OIG grant to R.J. and D.F.

Correspondence and requests for materials should be addressed to P.C. (e-mail: Peter.Carmeliet@med.kuleuven.ac.be).

Tests of quantum gravity from observations of γ-ray bursts

G. Amelino-Camelia*†, John Ellis‡, N. E. Mavromatos*, D. V. Nanopoulos§ & Subir Sarkar*

** Theoretical Physics, University of Oxford, 1 Keble Road, Oxford OX1 3NP, UK*
† Institut de Physique, Université de Neuchâtel, CH-2000 Neuchâtel, Switzerland
‡ Theory Division, CERN, CH-1211 Geneva, Switzerland
§ Academy of Athens, Chair of Theoretical Physics, Division of Natural Sciences, 28 Panepistimiou Avenue, Athens GR-10679, Greece; Center for Theoretical Physics, Department of Physics, Texas A & M University, College Station, Texas 77843-4242, USA; and Astroparticle Physics Group, Houston Advanced Research Center (HARC), The Mitchell Campus, Woodlands, Texas 77381, USA

The recent confirmation that at least some γ-ray bursts originate at cosmological distances[1–4] suggests that the radiation from them could be used to probe some of the fundamental laws of physics. Here we show that γ-ray bursts will be sensitive to an energy dispersion predicted by some approaches to quantum gravity. Many of the bursts have structure on relatively rapid timescales[5], which means that in principle it is possible to look for energy-dependent dispersion of the radiation, manifested in the arrival times of the photons, if several different energy bands are observed simultaneously. A simple estimate indicates that, because of their high energies and distant origin, observations of these bursts should be sensitive to a dispersion scale that is comparable to the Planck energy scale ($\sim 10^{19}$ GeV), which is sufficient to test theories of quantum gravity. Such observations are already possible using existing γ-ray burst detectors.

Our interest is in the search for possible *in vacuo* dispersion, $\delta v \approx E/E_{QG}$, of electromagnetic radiation from γ-ray bursts (GRBs), which could be sensitive to a type of candidate quantum-gravity effect that has been recently considered in the particle-physics literature. (Here E is the photon energy and E_{QG} is an effective quantum-gravity energy scale). This candidate quantum-gravity effect would be induced by a deformed dispersion relation for photons of the form $c^2\mathbf{p}^2 = E^2[1 + f(E/E_{QG})]$, where f is a model-dependent function of the dimensionless ratio E/E_{QG}, $\mathbf{p}$ is the photon momentum and c is the velocity of light. In quantum-gravity models in which the hamiltonian equation of motion $\dot{x}_1 = \partial H/\partial p_1$ is still valid at least approximately, as in the frameworks discussed later, such a deformed dispersion relation would lead to energy-dependent velocities $c + \gamma v$ for massless particles, with implications for all the electromagnetic signals that we receive from astrophysical objects at large distances. At small energies $E \ll E_{QG}$, we expect that a series expansion of the dispersion relation should be applicable: $c^2\mathbf{p}^2 = E^2[1 + \xi E/E_{QG} + O(E^2/E_{QG}^2)]$, where $\xi = \pm 1$ is a sign ambiguity that would be fixed in a given dynamical framework. Such a series expansion would correspond to energy-dependent velocities:

$$v = \frac{\partial E}{\partial p} \approx c\left(1 - \xi\frac{E}{E_{QG}}\right) \qquad (1)$$

This type of velocity dispersion results from a picture of the vacuum as a quantum-gravitational 'medium', which responds differently to the propagation of particles of different energies and hence velocities. This is analogous to propagation through a conventional medium such as an electromagnetic plasma[6]. The gravitational 'medium' is generally believed to contain microscopic quantum fluctuations, which may occur on scale sizes of order the Planck length $L_P \approx 10^{-33}$ cm on timescales of the order of $t_P \approx 1/E_P$, where $E_P \approx 10^{19}$ GeV. These may[7,8] be analogous to the thermal fluctuations in a plasma, that occur on timescales of the order of $t \approx 1/T$, where T is the temperature. As it is a much 'harder' phenomenon associated with new physics at an energy scale far beyond typical photon energies, any analogous quantum-gravity effect could be distinguished by its different energy dependence: the quantum-gravity effect would increase with energy, whereas conventional medium effects decrease with energy in the range of interest[6].

Equation (1) encodes a minute modification for most practical purposes, as E_{QG} is believed to be a very high scale, presumably of the order of the Planck scale $E_P \approx 10^{19}$ GeV. Even so, such a deformation could be rather significant for even moderate-energy signals, if they travel over very long distances. According to equation (1), a signal of energy E that travels a distance L acquires a 'time delay', measured with respect to the ordinary case of an energy-independent speed c for massless particles:

$$\Delta t \approx \xi\frac{E}{E_{QG}}\frac{L}{c} \qquad (2)$$

This is most likely to be observable when E and L are large while the interval δt, over which the signal exhibits time structure, is small. This is the case for GRBs, which is why they offer particularly good prospects for such measurements, as we discuss later.

We first review briefly how modified laws for the propagation of particles have emerged independently in different quantum-gravity approaches. The suggestion that quantum-gravitational fluctuations might modify particle propagation in an observable way can already be found in refs 7 and 9. A phenomenological parametrization of the way this could affect the neutral kaon system[9–11] has been already tested in laboratory experiments, which have set lower limits on parameters analogous to the E_{QG} introduced above at levels comparable to E_P (ref. 12). In the case of massless particles such as the photon, which interests us here, the first example of a quantum-gravitational medium effect with which we are familiar occurred in a string formulation of an expanding Robertson–Walker–Friedman cosmology[13], in which photon propagation appears tachyonic. Deformed dispersion relations that are consistent with the specific formula in equation (1) arose in approaches based on quantum deformations of Poincaré symmetries[14] with a dimensional parameter. Within this general class of deformations, one finds[14,15] an effect consistent with equation (1) if the deformation is rotationally invariant: the dispersion relation for massless particles $c^2\mathbf{p}^2 = E_{QG}^2[1 - \exp(E/E_{QG})]^2$, and therefore $\xi = 1$. We noted that a deformed dispersion relation has also been found in studies of the quantization of point particles in a discrete space time[16].

A specific and general dynamical framework for the emergence of the velocity law (equation (1)) has emerged[17] within the Liouville string approach[7] to quantum gravity, according to which the vacuum is viewed as a non-trivial medium containing 'foamy' quantum-gravity fluctuations. The nature of this foamy vacuum may be visualized by imagining processes that include the pair creation of virtual black holes. Within this approach, it is possible to verify that massless particles of different energies excite vacuum fluctuations differently as they propagate through the quantum-gravity medium, giving rise to a non-trivial dispersion relation of Lorentz 'non-covariant' form, just as in a thermal medium. The form of the dispersion relation is not known exactly, but its structure has been studied[17] via a perturbative expansion, and it was shown in ref. 17 that the leading $1/E_{QG}$ correction is in agreement with equation (1).

It has been recently suggested[8] the vacuum might have analogous 'thermal' properties in a large class of quantum-gravity approaches, namely all approaches in which a minimum length L_{min}—such as the Planck length $L_P \approx 10^{-33}$ cm—characterizes short-distance physics. These should in general lead to deformed photon dispersion relations with $E_{QG} \approx 1/L_{min}$, though the specific form of equation (1) may not hold in all models, and hence may be used to discriminate between them. In support of equation (1), though, we recall[15,17] that this type of non-trivial dispersion in the quantum-gravity vacuum has implications for the measurability of distances in quantum gravity that fit well with the intuition emerging from

recent heuristic analyses[18] based on a combination of arguments from ordinary quantum mechanics and general relativity.

We now explain how GRBs provide an excellent way of testing such ideas, now that the cosmological origin of at least some of them has been established. We recall that typical photon energies in GRB emissions are[5] in the range 0.1–100 MeV, and it is possible that the spectrum might in fact extend up to TeV energies[19]. Moreover, time structure down to the millisecond scale has been observed in the light curves[5], as is predicted in the most popular theoretical models[20] involving merging neutron stars or black holes, where the last stages occur on the timescales associated with grazing orbits. Similar timescales could also occur in models that identify GRBs with other cataclysmic stellar events, such as failed supernovae of type Ib, young ultra-magnetized pulsars or the sudden deaths of massive stars[21]. We see from equations (1) and (2) that a signal with millisecond time structure in photons of energy ~20 MeV coming from a distance of the order of 10^{10} light yr, which is well within the range of GRB observations and models, would be sensitive to E_{QG} of the order of 10^{19} GeV $\approx 1/L_P$.

Significant sensitivities may already be attainable with the present GRB data. Submillisecond time-structure has been seen[22] in GRB 910711, and a recent time-series analysis[23] of the light curve of GRB 920229 using the bayesian block technique has identified a narrow microburst with a rise and decay timescale of the order of 100 μs. This is seen simultaneously in three (of the available four) energy channels of the BATSE detector on board the Compton Gamma Ray Observatory, covering the energy regions 20–50 keV, 50–100 keV and 100–300 keV, respectively. From the time structure of this microburst we think it should be possible to extract an upper limit of $\Delta t \leqslant 10^{-2}$ s on the difference in the arrival times of the burst at energies separated by $\Delta E \approx 200$ keV. If a burst such as this were to be demonstrated in the future to lie at a redshift $z \approx 1$, as seems quite plausible, the implied sensitivity would be to $E_{QG} \approx 10^{16}$ GeV, and it would be possible to improve this to $\sim 10^{17}$ GeV if the time difference could be brought down to the rise time reported in ref. 23. We note in passing that the simultaneous arrival of photons of different energies from such a large distance also imposes an upper limit of the order of 10^{-6} eV on a possible photon mass, but this is much less stringent than other astrophysical and laboratory limits[24].

These levels of sensitivity are even more interesting in light of the fact that recent theoretical work on quantum gravity, particularly within string theory, appears to favour values of the effective scale characterizing the onset of significant quantum-gravity effects that are somewhat below the Planck scale, typically in the range 10^{16}–10^{18} GeV (ref. 25). If our scale E_{QG} were indeed to be given by such an effective quantum-gravity scale, parts of the GRB spectrum with energies around 0.1 MeV and millisecond time structure (or energies of the order of 100 MeV and 1-s time structure, or energies around 1 TeV and 1-h time structure) might be sensitive to the type of candidate quantum-gravity phenomenon discussed here.

To provide some quantitative comparison of the GRB sensitivity to this phenomenon with that of other astrophysical phenomena, we can compare values of the 'sensitivity factor' $\eta \equiv |\Delta t^*|/\delta t$, where δt represents the time structure of the signal, and Δt^* is the time delay acquired by the signal if $E_{QG} \approx E_P$, namely $\Delta t^* \approx \pm EL/(cE_P)$. As already discussed, GRB emission with millisecond time structure and energy around 20 MeV that travels a distance of the order of 10^{10} light yr has $\eta \approx 1$. Another interesting possibility is that we may observe lensing of a GRB by a foreground galaxy[26,27]. The burst would then reach us by two or more different paths whose light travel times would differ typically by weeks to years. As conventional gravitational lensing is achromatic, any energy-dependence in the time delay would be a direct probe of the new physics of interest, and would be independent of the actual emission mechanism of γ-ray bursts. We note that the HEGRA[28] and Whipple[29] air Čerenkov telescopes have already searched for TeV emission from the direction of GRBs, motivated by the EGRET telescope's detection[30] of emission up to 18 GeV from GRB940217. If such searches were to prove successful and moreover, identified a lensed GRB, one would be able to infer via equation (2) a sensitivity factor down to $\eta \approx 10^{-6}$.

As observed in ref. 17, which did not consider GRBs as the cosmological distances of these phenomena were not then established, pulsars and supernovae are among the other astrophysical phenomena that might at first sight appear well suited for probing the physics we are interested in here, because of the short time structures they display. However, although pulsar signals have very well-defined time structure, they are at relatively low energies and are observable over distances of at most 10^4 light yr. If one takes an energy of the order of 1 eV and postulates a sensitivity to time delays as small as 1 μs, one estimates a sensitivity down to $\eta \approx 10^{-10}$. With new experiments such as AXAF it may be possible to detect X-ray pulsars out to 10^6 light years, allowing us to probe down to $\eta \approx 10^{-8}$.

We note that neutrinos from type-II supernovae like SN1987a—which should have energies up to ~100 MeV with a time structure that could extend down to milliseconds—are likely to be detectable at distances of up to $\sim 10^5$ light yr, providing sensitivity down to $\eta \approx 10^{-4}$. We have also considered the cosmic microwave background. Although the distance travelled by these photons is the largest available, the only possible signature is a small distortion of the Planck spectrum due to the frequency-dependence of c, which we estimate to be of the order of $\Delta I(\nu)/I(\nu) \approx \nu/E_P \approx 10^{-32}$, where $I(\nu)$ is the frequency spectrum, which is negligible.

In principle, GRBs allow us to gain many orders of magnitude in the sensitivity factor η. Moreover, and most importantly, this high sensitivity should be sufficient to probe values of the effective scale characterizing the onset of quantum-gravity effects extending all the way up to the Planck scale, as illustrated by the estimates we have provided. Ideally, one would like to understand well the short-time structure of GRB signals in terms of conventional physics, so that the phenomena discussed here may be disentangled unambiguously. However, even in the absence of a complete theoretical understanding, sensitive tests can be performed as indicated above, through the serendipitous detection of short-scale time structure[23] at different energies in GRBs which are established to be at cosmological distances. Detailed features of burst time series should enable the emission times in different energy ranges to be put into correspondence. As any time shift due to quantum-gravity effects of the type discussed here would increase with the photon energy, this characteristic dependence should be separable from more conventional in-medium physics effects, which decrease with energy. To distinguish any quantum-gravity shift from effects due to the source, we recall that the medium effect would be linear in the source distance and in the photon energy, which would not in general be the case for time shifts at the source. To disentangle any such effects, it is clear that the most desirable features in an observational programme would be fine time resolution at high photon energies. □

Received 12 December 1997; accepted 10 April 1998.

1. van Paradis, J. *et al.* Transient optical emission from the error box of the γ-ray burst of 28 February 1997. *Nature* **386,** 686–689 (1997).
2. Groot, P. J. *et al. IAU Circ.* No. 6676 (1997).
3. Metzger, M. L. *et al.* Spectral constraints on the redshift of the optical counterpart to the γ-ray burst of 8 May 1997. *Nature* **387,** 878–880 (1997).
4. Metzger, M. L. *et al. IAU Circ.* No. 6676 (1997).
5. Fishman, G. J. & Meegan, C. A. Gamma-ray bursts. *Annu. Rev. Astron. Astrophys.* **33,** 415–458 (1995).
6. Latorre, J. I., Pascual, P. & Tarrach, R. Speed of light in nontrivial vacua. *Nucl. Phys. B* **437,** 60–82 (1995).
7. Ellis, J., Mavromatos, N. & Nanopoulos, D. V. String theory modifies quantum mechanics. *Phys. Lett. B* **293,** 37–48 (1992).
8. Garay, L. J. Space-time foam as a quantum thermal bath. *Phys. Rev. Lett.* (submitted); also as preprint gr-qc/9801024.
9. Ellis, J., Hagelin, J. S., Nanopoulos, D. V. & Srednicki, M. Search for violations of quantum mechanics. *Nucl. Phys. B* **241,** 381–405 (1984).
10. Ellis, J., Lopez, J., Mavromatos, N. & Nanopoulos, D. V. Precision tests of CPT symmetry and quantum mechanics in the neutral kaon system. *Phys. Rev. D* **53,** 3846–3870 (1996).
11. Huet, P. & Peskin, M. E. Violation of CPT and quantum mechanics in the $K_0 - \bar{K}_0$ system. *Nucl. Phys. B* **434,** 3–38 (1995).
12. Adler, R. *et al.* Tests of CPT symmetry and quantum mechanics with experinental data from CPLEAR. *Phys. Lett. B* **364,** 239–245 (1995).

13. Antoniadis, I., Bachas, C., Ellis, J. & Nanopoulos, D. V. Comments on cosmological string solutions. *Phys. Lett. B* **257,** 278–284 (1991).
14. Lukierski, J., Nowicki, A. & Ruegg, H. Classical and quantum-mechanics of free κ-relativistic systems. *Ann. Phys.* **243,** 90–116 (1995).
15. Amelino-Camelia, G. Enlarged bound on the measurability of distances and quantum κ-Poincaré group. *Phys. Lett. B* **392,** 283–286 (1997).
16. 't Hooft, G. Quantization of point particles in (2 + 1)-dimensional gravity and space-time discreteness. *Class. Quant. Grav.* **13,** 1023–1039 (1996).
17. Amelino-Camelia, G., Ellis, J., Mavromatos, N. E. & Nanopoulos, D. V. Distance measurement and wave dispersion in a Liouville string approach to quantum gravity. *Int. J. Mod. Phys. A* **12,** 607–623 (1997).
18. Amelino-Camelia, G. Limits on the measurability of space-time distances in the semi-classical approximation of quantum gravity. *Mod. Phys. Lett. A* **9,** 3415–3422 (1994).
19. Baring, M. G. Gamma-ray bursts above 1 GeV. in *Towards a Major Atmospheric Cerenkov Detector* (ed. de Jager, O. C.) (Proc. Kruger National Park TeV Workshop, Westprint, Potchefstroom, in the press); also as preprint astro-ph/9711256.
20. Rees, M. J. Gamma-ray bursts: challenges to relativistic astrophysics. in *Proc. 18th Texas Symp. on Relativistic Astrohysics 1996* (eds Olinto, A., Friemann, J. & Schramm, D. N.) (World Scientific, in the press); also as preprint astro-ph/9701162.
21. Mészáros, P. Theoretical models of gamma-ray bursts. in *Gamma-Ray Bursts* (eds Meegan, C., Preece, R. & Koshut, T.) (Proc. 4th Huntsville Symp., Am. Inst. Phys., in the press); also as preprint astro-ph/9711354.
22. Bhat, C. L. *et al.* Evidence for sub-millisecond structure in a γ-ray burster. *Nature* **359,** 217–216 (1992).
23. Scargle, J. D., Norris, J. & Bonnell, J. Attributes of GRB pulses: Bayesian blocks analysis of TTE data; a microburst in GR920229. in *Gamma-Ray Bursts* (eds Meegan, C., Preece, R. & Koshut, T.) (Proc. 4th Huntsville Symp., Am. Inst. Phys., in the press); also as preprint astro-ph/9712016.
24. Barnett, R. M. *et al.* Review of particle properties. *Phys. Rev. D* **54,** 207–720 (1996).
25. Witten, E. Strong coupling expansion of Calabi-Yau compactification. *Nucl. Phys. B* **471,** 135–158 (1996).
26. Paczynski, B. Gamma-ray bursts at cosmological distances. *Astrophys. J.* **308,** L43–L46 (1986).
27. Nemiroff, R. J. *et al.* Searching gamma-ray bursts for gravitational lensing echoes—Implications for compact dark matter. *Astrophys. J.* **414,** 36–40 (1994).
28. Krawczynski, H. *et al.* Search for TeV counterparts of gamma-ray bursts with the HEGRA experiment. in *Proc. Int. School of Cosmic-Ray Astrophysics* (World Scientific, in the press); also as preprint astro-ph/9611044.
29. Boyle, P. J. *et al.* in *Proc. 25th Int. Cosmic ray Conf.* Vol. 3 (eds Potgieter M. S. *et al.*) 61 (Westprint, Potchefstroom, 1998); also as preprint astro-ph/9706132.
30. Hurley, K. *et al.* Detection of a γ-ray burst of very long duration and very high energy. *Nature* **372,** 652–654 (1994).

Acknowledgements. G.A.-C. thanks J. Binney and other members of the Oxford Theoretical Astrophysics group for discussions. This work was supported in part by the Foundation Blanceflor Boncompagni-Ludovisi (G.A.-C), a PPARC advanced fellowship (N.E.M.) and the US Department of Energy (D.V.N.)

Correspondence and requests for materials should be addressed to G.A.-C. at the University of Neuchatel (e-mail: Giovanni.Amelino-Camelia@cern.ch).

Global warming on Triton

J. L. Elliot*†‡, H. B. Hammel*, L. H. Wasserman‡, O. G. Franz‡, S. W. McDonald*, M. J. Person*, C. B. Olkin‡, E. W. Dunham‡, J. R. Spencer‡, J. A. Stansberry‡, M. W. Buie‡, J. M. Pasachoff§, B. A. Babcock‖ & T. H. McConnochie§

** Department of Earth, Atmospheric, and Planetary Sciences, † Department of Physics, Massachusetts Institute of Technology, Cambridge, Massachusetts 02139-4307, USA*
‡ Lowell Observatory, Flagstaff, Arizona 86001, USA
§ Astronomy Department, ‖ Physics Department, Williams College, Williamstown, Massachusetts 01267-2565, USA

Triton, Neptune's largest moon, has been predicted to undergo significant seasonal changes that would reveal themselves as changes in its mean frost temperature[1–3]. But whether this temperature should at the present time be increasing, decreasing or constant depends on a number of parameters (such as the thermal properties of the surface, and frost migration patterns) that are unknown. Here we report observations of a recent stellar occultation by Triton which, when combined with earlier results, show that Triton has undergone a period of global warming since 1989. Our most conservative estimates of the rate of temperature and surface-pressure increase during this period imply that the atmosphere is doubling in bulk every 10 years—significantly faster than predicted by any published frost model for Triton[2,3]. Our result suggests that permanent polar caps on Triton play a dominant role in regulating seasonal atmospheric changes. Similar processes should also be active on Pluto.

The 4 November 1997 occultation of the star Tr180 (also known as Tycho 651672 and GSC6321–01030) was successfully observed with the Hubble Space Telescope (HST) in daylight over the northwest Pacific Ocean; Astrometer 3 of the Fine Guidance Sensors (FGS) was used to record the event[5]. Details of the HST data are given in Table 1 along with information about other observing stations; the immersion and emersion data (disappearance and reappearance of the star) are shown in Fig. 1. A central flash (the focusing of light rays by Triton's atmosphere[6,7]) was recorded, but will be presented and analysed elsewhere.

We modelled the HST light curve with a standard small-planet model that allows for a power-law temperature gradient[8] (Table 2). The background from dark counts and Triton (determined by the FGS in September and adjusted for Triton's different distance) was subtracted, and the remainder was divided by the flux from the star (also determined by the FGS in September) so that the full range of stellar flux corresponded to values between 0.0 and 1.0. In the light-curve model fits, the zero level was fixed, but the full-scale signal from the star was a free parameter. The difference of the fitted values from 1.0 shows that our calibration error is only a few tenths of one per cent.

From fitting the entire light curve, the closest-approach distance between the centre of Triton's shadow and the HST was determined to be 224 ± 4 km (first column of results in Table 2). This value places the shadow somewhat further north than predicted, but it is consistent with no detectable occultation at our Oahu station (Table 1). Using the closest-approach distance determined from the entire light curve, we fitted the main immersion and emersion sections of the light curve both separately and together (next three columns of results in Table 2). As a test of the self-consistency of our light-curve models, we fixed the atmospheric model parameters ("half-light radius", "lambda at half-light," and the "thermal-gradient exponent"; see ref. 8) at their values determined from

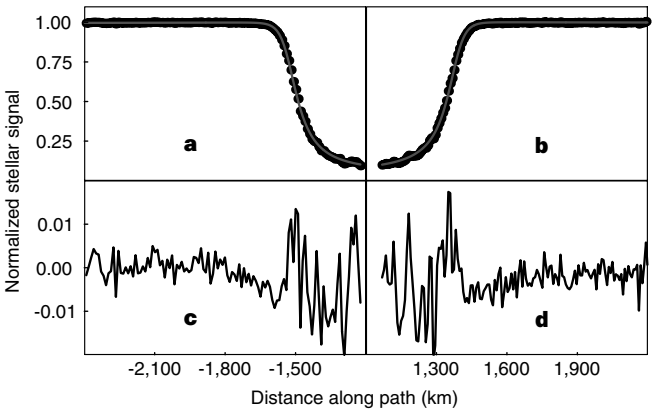

Figure 1 Triton occultation light curves from the HST. Data before and after the occultation were used to establish the modulation of the signal due to the astrometer scan, which was then removed from the entire data set. The zero and full-scale stellar flux levels were established with photometric data from an earlier FGS visit to these objects on 11 September 1997. At that time, Triton's magnitude as observed by the FGS was 13.4 and the magnitude of Tr180 was 10.6. The FGS data have been averaged at 1.0 s; **a**, immersion data (filled circles) and light-curve model fit (line); **b**, emersion data (filled circles) and light-curve model fit (line; see fits in Table 2). The zero point of the abscissa is arbitrary. The light-curve model[8] used a power-law thermal gradient; residuals from the fit in **a** are shown in **c**, and the residuals from the fit in **b** are shown in **d**. The r.m.s. residual along the full signal is ~0.0022 for a 1-s average, and is the result of photon noise. The remaining residuals that occur when the star is partially occulted are the result of unmodelled structure in Triton's atmosphere and rarely exceed 0.01. The effect of these on our determination of the 1,400-km pressure can be estimated by differences among the fits in Table 1. The omitted central portion of the light curve (see text) corresponds to radii <1,400 km (altitudes <48 km); the atmosphere below that does not affect the 1,400-km pressure.

Immunofluorescence assay. For latent KSHV antigens, cytospin preparations were fixed with methanol/acetone, and incubated with KS sera at a 1:40 dilution in master block as described[19], followed by incubation with an FITC-conjugated $F(ab')_2$ fragment of rabbit anti-human IgG (DAKO). For lytic antigens, cytospin preparations of TPA-induced cells were fixed and incubated either overnight at 4 °C with mAb 11D1 (ref. 12; gift from B. Chandran), which is specific for the DNA-replication protein ORF 59, at a dilution of 1:10, or for 1 h at room temperature with a polyclonal rabbit antibody raised against the main capsid protein ORF 25 (gift from S. J. Gao) and diluted 1:300, followed by 40 min incubation with an FITC-conjugated goat $F(ab)'_2$ fragment to either mouse IgG (ICN Biomedicals) or rabbit IgG (Jackson ImmunoResearch). Cell nuclei were counterstained with DAPI (4′-6′-diamino-2′-phenylindole dihydrochloride; Boehringer Mannheim), and examined in a fluorescence microscope (Axioplan 2; Zeiss).

Cell-proliferation assay. Infected and uninfected HUVECs were washed and cultured at 10^4 cells per 200 μl in serum-free medium (X-vivo 20) containing no VEGF, or 20 ng ml^{-1} or 40 ng ml^{-1} VEGF for 24 h. Cells were then pulsed with ^{3}H-thymidine, maintained in culture for 36 h, collected and counted in a β-scintillation counter. Values represent the mean ± standard deviation c.p.m. ^{3}H-thymidine incorporated for triplicate cultures.

Telomerase assay. The radioactive TRAP assay for telomerase activity has been described[16,20].

Anchorage-independent growth. 2 × M 199 medium (BioWhittaker) with 2 × ECGS (endothelial growth supplement, PerImmune, Inc.) and 40% fetal calf serum (FCS) were mixed with an equal amount of 0.8% melted agar and 1 ml was poured into each 35-mm plate to form a bottom layer; then 2 × M 199 with 2 × ECGF and 40% FCS were mixed with an equal amount of 0.4% melted agar and 1 ml was added to serial concentrations of cells (10^3, 10^4, 10^5) and poured over the bottom layer to form a top layer.

Cytokine and chemokine assays. Assays were done by ELISA in a commercial laboratory (Cytokine Core Laboratory).

Flow cytometer analysis. FITC conjugated mAbs (PECAM, E-selectin, VCAM, ICAM) were used as described[8]. KDR expression was quantified by a FITC-conjugated mAb to KDR (clone 6.64, VEGF-binding domain) (gift from ImClone Systems).

Received 30 March; accepted 11 June 1998.

1. Chang, Y. *et al.* Identification of herpesvirus-like DNA sequences in AIDS-associated Kaposi's sarcoma. *Science* **266,** 1865–1869 (1994).
2. Moore, P. S. & Chang, Y. Detection of herpesvirus-like DNA sequences in Kaposi's sarcoma in patients with and those without HIV infection. *N. Engl. J. Med.* **332,** 1181–1185 (1995).
3. Boshoff, C. *et al.* Kaposi's sarcoma-associated herpesvirus infects endothelial and spindle cells. *Nature Med.* **1,** 1274–1278 (1995).
4. Reed, J. A. *et al.* Demonstration of Kaposi's sarcoma-associated herpesvirus cyclin D homolog in cutaneous Kaposi's sarcoma by colorimetric *in situ* hybridization using a catalyzed signal amplification system. *Blood* (in the press).
5. Arvanitakis, L. *et al.* Establishment and characterization of a primary effusion (body cavity-based) lymphoma cell line (BC-3) harboring Kaposi's sarcoma-associated herpesvirus (KSHV/HHV-8) in the absence of Epstein–Barr virus. *Blood* **88,** 2648–2654 (1996).
6. Renne, R. *et al.* Lytic growth of Kaposi's sarcoma-associated herpesvirus (human herpesvirus 8) in culture. *Nature Med.* **2,** 342–346 (1996).
7. Miller, G. *et al.* Selective switch between latency and lytic replication of Kaposi's sarcoma herpesvirus and Epstein–Barr virus in dually infected body cavity lymphoma cells. *J. Virol.* **71,** 314–324 (1997).
8. Rafii, S. *et al.* Human bone marrow microvascular endothelial support long term proliferation and differentiation of myeloid and megakaryocytic progenitors. *Blood* **86,** 3353–3363 (1995).
9. Watanabe, Y. & Dvorak, H. F. Vascular permeability factor/vascular endothelial growth factor inhibits anchorage-disruption-induced apoptosis in microvessel endothelial cells by inducing scaffold formation. *Exp. Cell Res.* **233,** 340–349 (1997).
10. Cesarman, E. *et al.* Kaposi's sarcoma associated herpesvirus (KSHV/HHV-8) contains G protein-coupled receptor and cyclin D homologs which are expressed in Kaposi's sarcoma and malignant lymphoma. *J. Virol.* **70,** 8218–8223 (1996).
11. O'Leary, J. *PCR In-situ Hybridization.* 1-53-86 (IRL, Oxford University Press, Oxford, 1997).
12. Ruby Chan, S., Bloomer, C. & Chandran, B. Identification and characterization of human herpesvirus-8 lytic cycle associated ORF 59 protein and the encoding cDNA by monoclonal antibody. *Virology* **240,** 118–126 (1998).
13. Hewett, P. W. & Murray, J. C. Coexpression of flt-1, flt-4 and KDR in freshly isolated and cultured human endothelial cells. *Biochem. Biophys. Res. Commun.* **221,** 697–702 (1996).
14. Rienke, U., Burlington, H., Cronkite, E. P. & Laissue, J. Hayflick's hypothesis: an approach to *in vivo* testing. *Fed. Proc.* **34,** 71–75 (1975).
15. Kim, N. W. *et al.* Specific association of human telomerase activity with immortal cells and cancer. *Science* **266,** 2011–2015 (1994).
16. Mieczyslaw, A. P. *et al.* Detection of telomerase activity in human cells and tumors by a telomeric repeat amplification protocol (TRAP). *Meth. Cell Sci.* **17,** 1–15 (1995).
17. Kennedy, M. M. *et al.* HHV8 and Kaposi's sarcoma: a time cohort study. *Mol. Pathol.* **50,** 96–100 (1997).
18. Rhoads, R. E. Optimization of the annealing temperature for DNA amplification *in vitro*. *Nucleic Acids Res.* **18,** 6409–6412 (1990).
19. Kedes, D. H. *et al.* The seroepidemiology of human herpesvirus 8 (Kaposi's sarcoma-associated herpesvirus): Distribution of infection in KS risk groups and evidence for sexual transmission. *Nature Med.* **2,** 918–924 (1996).
20. Kim, N. W. & Wu, F. Advances in quantification and characterization of telomerase activity by the telomeric repeat amplification protocol (TRAP). *Nucleic Acids Res.* **25,** 2595–2597 (1997).

Supplementary information is available on *Nature*'s World-Wide Web site (http://www.nature.com) or as paper copy from the London editorial office of *Nature*.

Acknowledgements. We thank S. Chen-Kiang, D. Knowles, M. C. Gershengorn and E. Mesri for their suggestions; B. Chandran and S.-J. Gao for antibodies against lytic antigens; P. Pellet for positive controls CMB and HHV-6; L. Friedman, S. Nikolovska, B. Ferris, G. Lam, A. J. Naiyer, S. Diana, I. Silva and V. Uhlmann for technical help; and S. Picton and K. Lohman at Perkin Elmer Applied Biosystems.

Correspondence and requests for materials should be addressed to E.C. (e-mail: ecesarm@mail.med.cornell.edu).

Perinuclear localization of chromatin facilitates transcriptional silencing

Erik D. Andrulis, Aaron M. Neiman, David C. Zappulla & Rolf Sternglanz

Department of Biochemistry and Cell Biology, State University of New York at Stony Brook, Stony Brook, New York 11794-5215, USA

Transcriptional silencing in *Saccharomyces cerevisiae* at the *HM* mating-type loci and telomeres occurs through the formation of a heterochromatin-like structure. *HM* silencing is regulated by *cis*-acting elements, termed silencers, and by *trans*-acting factors that bind to the silencers. These factors attract the four SIR (silent information regulator) proteins, three of which (SIR2–4) spread from the silencers to alter chromatin, hence silencing nearby genes[1–4]. We show here that an *HMR* locus with a defective silencer can be silenced by anchoring the locus to the nuclear periphery. This was accomplished by fusing integral membrane proteins to the GAL4 DNA-binding domain and overproducing the hybrid proteins, causing them to accumulate in the endoplasmic reticulum and the nuclear membrane. We expressed the hybrid proteins in a strain carrying an *HMR* silencer with GAL4-binding sites (UAS_G) replacing silencer elements, causing the silencer to become anchored to the nuclear periphery and leading to silencing of a nearby reporter gene. This silencing required the hybrids of the GAL4 DNA-binding domain with membrane proteins, the UAS_G sites and the SIR proteins. Our results indicate that perinuclear localization helps to establish transcriptionally silent chromatin.

Yeast and *Drosophila* telomeres are probably located at the nuclear periphery[5–7], where some non-telomeric heterochromatin is also found[8]; however, it is unclear whether this localization contributes to the formation of heterochromatin or is a consequence of it. We tested whether genes artificially drawn to the yeast nuclear envelope could become transcriptionally silenced by using strains with an *HMR* locus in which UAS_G sites replaced some or all of the usual elements at the *HMR-E* silencer. This silencer normally contains three elements, A, E and B, that are binding sites for the proteins ORC, RAP1 and ABF1, respectively[9]. Deletion of any one of these elements leads to little or no derepression of *HMR*, whereas deletion of any two elements leads to full derepression[9]. If these silencer elements are replaced by UAS_G sites, silencing is lost, but it can be restored by the introduction of any one of several different GAL4 DNA-binding domain (G_{BD}) hybrids, including those with SIR1, SIR3, SIR4, RAP1 and ORC1 (refs 2, 10–12): we refer to this as targeted silencing. We used the same strategy to assess the role of perinuclear localization in silencing. As overexpression of Golgi proteins leads to their accumulation in the endoplasmic reticulum (ER) and the nuclear membrane[13,14], we investigated whether overexpressed G_{BD}–Golgi protein hybrids could cause targeted silencing.

First, we tested YIP1, an essential protein with at least three predicted membrane-spanning domains. YIP1 is a Golgi protein

involved in ER-to-Golgi and/or early Golgi membrane transport (D. Gallwitz, personal communication). Indirect immunofluorescence showed that when G_{BD}–YIP1 was overproduced, nuclear rim staining appeared (Fig. 1) that was consistent with accumulation in the ER and the nuclear membrane. In contrast, G_{BD} alone was seen throughout the nucleoplasm, coincident with DAPI staining.

We tested the G_{BD}–YIP1 hybrid in three targeted silencing strains[10], which differed only in the specific silencer elements deleted from the *HMR-E* silencer. A cell-spotting assay was used to quantify the extent of silencing of an *hmr::TRP1* reporter gene. Lack of growth on a medium without tryptophan demonstrates silencing in this assay. The G_{BD}–YIP1 hybrid gave silencing in strain YSB35 (Fig. 2a, row 1), which has the RAP1- and ABF1-binding sites deleted from the *HMR-E* silencer. This hybrid also gave silencing in strain YSB2, which has the ORC- and RAP1-binding sites deleted (Fig. 2b, row 1), although there was less silencing than in YSB35 (compare rows 1 in Fig. 2a, b). This had been seen previously for G_{BD}–SIR1; it too gave better targeted silencing in YSB35 than in YSB2 (ref. 10).

Figure 2 also shows the effect of *sir* mutations in these strains. Silencing by G_{BD}–YIP1 was abolished in *sir2* and *sir3* derivatives of strain YSB35 and greatly weakened in a *sir1* mutant (Fig. 2a). Silencing by G_{BD}–YIP1 in strain YSB2 also depended on SIR2, SIR3 and SIR4, but was barely affected by a *sir1* mutation (Fig. 2b, and data not shown). The silencing also depended on the presence of the UAS_G sites (Fig. 2d), and thus had all the hallmarks of targeted silencing (demonstrated previously by proteins directly involved in silencing)[2,10–12].

There was no silencing for G_{BD}–YIP1 in strain YSB41, which has all three elements deleted from the *HMR-E* silencer (Fig. 2c), in contrast to G_{BD}–SIR1, which gave some silencing in this strain[2] (Fig. 2c). Thus, targeted silencing by this membrane protein required the presence of at least one natural silencer element.

To test the generality of these results with G_{BD}–YIP1, we tested four other membrane proteins. We identified two as YIP1-interacting proteins in a two-hybrid screen, YIF1 and YIP3. YIP3 is also involved in ER-to-Golgi membrane transport (D. Gallwitz, personal communication). It has two predicted membrane-spanning domains, whereas YIF1 has three. The other two proteins tested were MNN10, a Golgi mannosyltransferase[15], and STT3, a resident ER protein that is part of the oligosaccharyltransferase complex[16,17]. In the case of MNN10, overexpression leads to accumulation of the protein in the ER membrane (N. Dean, personal communication). As the N termini of both membrane proteins are likely to be cytoplasmic rather than lumenal[15,16], overexpression of G_{BD} hybrids of these proteins should cause their N termini to reside in the cytoplasm and/or nucleoplasm. All four membrane-protein hybrids caused repression of the *hmr::TRP1* reporter gene in strain YSB35 (Fig. 3a). Quantitative measurements showed that the degree of targeted silencing for the YIF1 hybrid was as good as, or better than, that of SIR1. The MNN10, YIP1 and YIP3 hybrids each gave less silencing than SIR1 and YIF1 (see Supplementary Information); the STT3 hybrid gave the least (Fig. 3). The silencing by these membrane-protein hybrids had all the features of targeted silencing, in that it required UAS_G sites and depended on SIR2, 3 and 4, as did G_{BD}–YIP1 (Fig. 2). All of the proteins gave better silencing in strain YSB35 than in YSB2, and none in YSB41, as did G_{BD}–YIP1 (Fig. 2).

We confirmed that this silencing was not due simply to overproduction of membrane proteins in the following experiment. As the N terminus of MNN10 is probably cytoplasmic, the G_{BD} domain

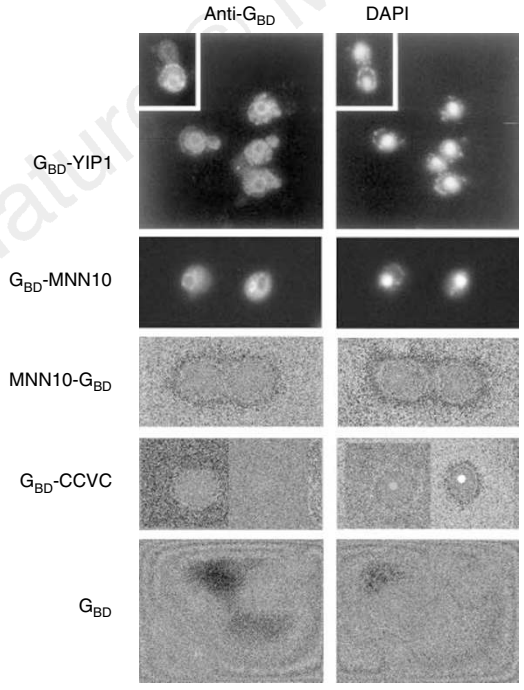

Figure 1 G_{BD} hybrids localized by indirect immunofluorescence. Cells were stained with DAPI (diamidino-2-phenylindole) to visualize the nuclei and with an anti-G_{BD} antibody to visualize G_{BD} and G_{BD} hybrids. DAPI staining shows the location of the nuclei and the mitochondria. Note that G_{BD} hybrids are observed at the nuclear rim and in some cases (inset) under the plasma membrane, consistent with ER localization[26].

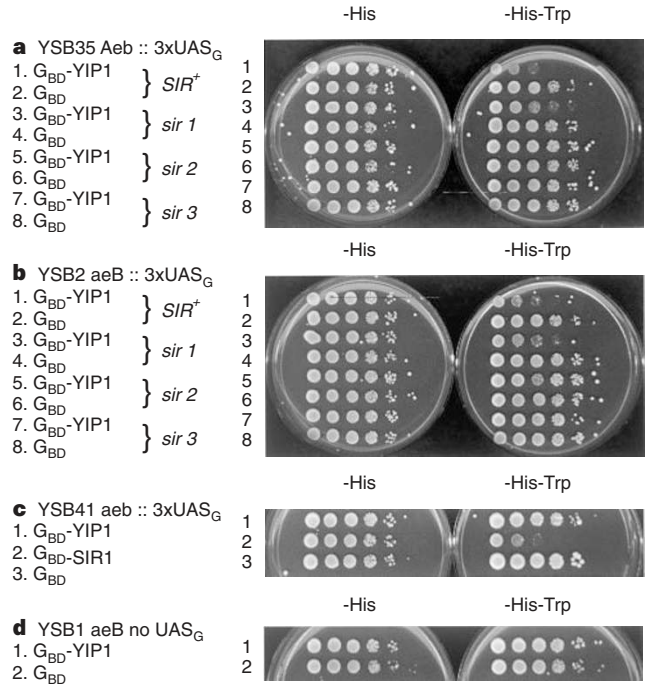

Figure 2 Targeted silencing by G_{BD}–YIP1. **a**, G_{BD}–YIP1 or G_{BD} was expressed in strain YSB35 (rows 1 and 2) or its *sir1* (rows 3 and 4), *sir2* (rows 5 and 6) or *sir3* (rows 7 and 8) derivatives. These strains have the E and B elements deleted from the *HMR-E* silencer and replaced by three UAS_G sites (designated Aeb)[10]. **b**, G_{BD}–YIP1 or G_{BD} was expressed in strain YSB2 (rows 1 and 2) or its *sir1* (rows 3 and 4), *sir2* (rows 5 and 6) or *sir3* (rows 7 and 8) derivatives. These strains have the A and E elements deleted from the *HMR-E* silencer and replaced with three UAS_G sites (designated aeB)[10]. **c**, G_{BD}–YIP1, G_{BD}–SIR1 or G_{BD} was expressed in strain YSB41. This strain has all three elements deleted from the *HMR-E* silencer and replaced with three UAS_G sites (designated aeb)[10]. **d**, G_{BD}–YIP1 or G_{BD} was expressed in strain YSB1. This strain has a similar silencer to the one in YSB2 (aeB, **b**), but has no UAS_G sites. In all cases, cell cultures were serially diluted 10-fold five times and 5 μl of each dilution spotted from left (no dilution) to right (10^5-fold dilution). Growth was assessed after two days at 30 °C. Targeted silencing is seen as a lack of growth on –His–Trp medium (for example, rows 1 and 3 in **a**, **b**, and row 2**c**).

of the G_{BD}–MNN10 hybrid, when it is overexpressed, should be in the nucleoplasm. As a control, we therefore constructed an MNN10 hybrid with G_{BD} at the C terminus (MNN10–G_{BD}). This protein would be expected to have G_{BD} in the lumen of the ER rather than in the nucleus, and thus would not be expected to give targeted silencing, which we found to be the case (Fig. 3b). This hybrid protein was expressed more than G_{BD}–MNN10 (Fig. 3b), and immunofluorescence experiments localized both MNN10 hybrids to the ER/nuclear membrane (Fig. 1).

We conclude that the G_{BD}–membrane protein hybrids, when overproduced, reside in the inner nuclear membrane and draw UAS_G sites to the nuclear periphery. We confirmed this by using a screen (to be described elsewhere) in which we looked for plasmids encoding G_{BD} hybrid proteins that would give targeted silencing in strain YEA76 (Aeb::3xUAS_G *hmr::URA3*). Among the plasmids found was one coding for G_{BD} fused to a tetrapeptide, Cys-Cys-Val-Cys (CCVC), followed by a stop codon; this tetrapeptide led to targeted silencing of a *URA3* reporter gene (Fig. 3c). The silencing did not occur in the same strain containing a *sir3* mutation. Furthermore, a frameshift mutation introduced at the junction between G_{BD} and the tetrapeptide abolished silencing (data not shown). As proteins with the sequence Cys-X-Cys (where X is any amino acid) at the C terminus are geranylgeranylated[18,19], we presume that the G_{BD}–CCVC hybrid was similarly modified; this modification then anchors the protein in the nuclear membrane (Fig. 1), where it facilitates targeted silencing in the same way as did the authentic membrane proteins. Thus, silencing is a consequence of anchorage to the periphery, rather than the attachment of a protein transmembrane domain to G_{BD} *per se*.

The membrane protein hybrids described here are unlikely to participate directly in silencing. Our data suggest that a membrane protein, when fused to G_{BD} and overexpressed, can bind to UAS_G sites on the chromosome and recruit nearby genes to the nuclear periphery. Why does such localization facilitate silencing? It has been suggested that the concentration of limiting SIR proteins is higher at the nuclear periphery[5,12,20], so recruitment to the periphery may rescue the silencing defect by increasing the local concentration of SIR proteins. One prediction of this model is that overproduction of SIR proteins may restore some silencing to partially defective silencers. Such overproduction can improve silencing in several contexts[20–22]. We found that overexpression of SIR4, and to a lesser extent SIR3, in strains YSB35 and YSB2 (Aeb and aeB silencers, respectively) caused some silencing (Fig. 4a, b). Furthermore, a combination of SIR3 or SIR4 overexpression, together with G_{BD}–YIP1, gave even greater silencing than did G_{BD}–YIP1 alone (Fig. 4). In strain YSB41, with all three silencer elements deleted from *HMR-E*, overexpression of SIR4 or SIR3 alone did not cause silencing (Fig. 4c), and neither did the membrane-protein hybrid G_{BD}–YIP1 (Figs 2c, 4c). However, the combination of SIR4 (or SIR3) overexpression plus G_{BD}–YIP1 did give silencing in this strain (Fig. 4c). These results support the idea that concentrations of SIR proteins are greater at the nuclear periphery, and are in agreement with previous immunofluorescence results[5]. We conclude that peri-

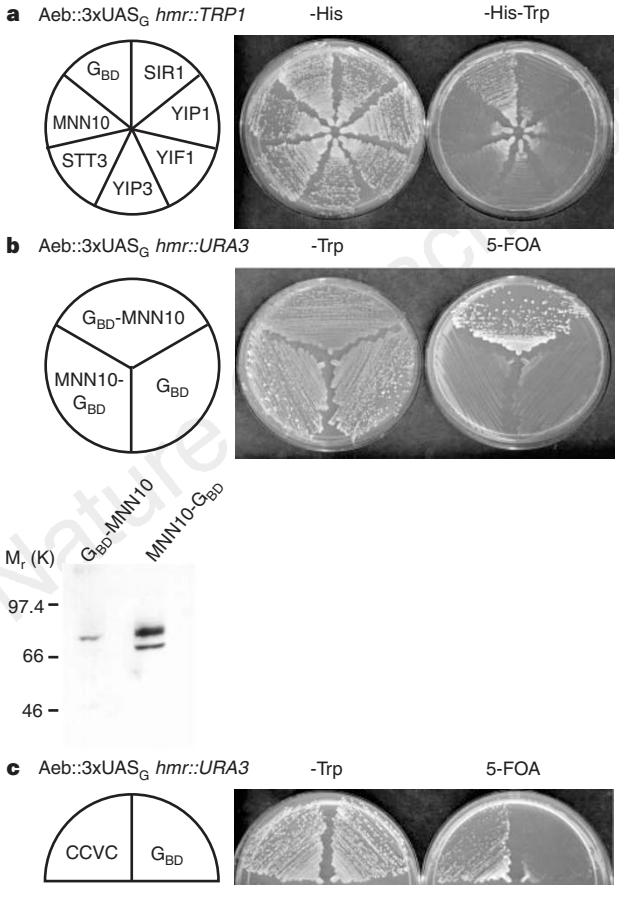

Figure 3 Several membrane protein hybrids give targeted silencing. **a**, Strain YSB35 expressing G_{BD}, G_{BD}-SIR1, G_{BD}-YIP1, G_{BD}-YIF1, G_{BD}-YIP3, G_{BD}-STT3 or G_{BD}-MNN10 was streaked either on –His medium (control) or on –His–Trp medium and growth assessed after two days at 30 °. Lack of growth on –His–Trp is indicative of silencing. **b**, Strain YEA76 (Aeb::3xUAS_G *hmr::URA3*) expressing G_{BD}-MNN10, MNN10-G_{BD}, or G_{BD} was streaked on –Trp medium (control) or on 5-fluoro-orotic acid (5-FOA)-containing medium. Growth on the latter medium is indicative of silencing. The lower panel shows a western blot of G_{BD}-MNN10 and MNN10-G_{BD} expressed in this strain. **c**, Strain YEA76 expressing G_{BD}-CCVC or G_{BD}. Silencing was assessed by growth on 5-FOA-containing medium as in **b**.

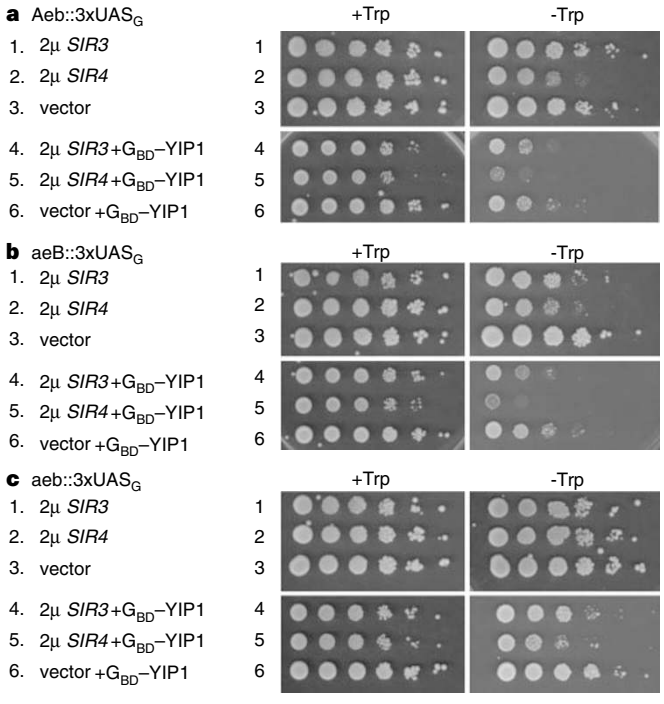

Figure 4 Overexpression of SIR3 and SIR4 improves silencing in strains with defective silencers. **a**, Strain YSB35; **b**, strain YSB2; **c**, strain YSB41. These strains are the same as the ones used for Fig. 2; they differ only in the nature of their silencers, as indicated. Strains with the indicated plasmids were serially diluted on control medium (–Ura in the case of one plasmid, or –Ura–His in the case of two plasmids; indicated as +Trp) or on medium lacking tryptophan (–Trp). As in Fig. 2, lack of growth on –Trp medium reflects silencing.

nuclear localization is important in establishing transcriptionally silent chromatin. □

Methods

Strains and plasmids. Strains YSB35, YSB2, YSB41 and YSB2 were used to measure targeted silencing as described[10]. All five membrane proteins were cloned in-frame into the overexpression vector pMA424 (ref. 23) to create G_{BD} hybrids. The entire coding sequence was used for YIP1 (pEDA73) and MNN10 (pEDA96). The YIP3 hybrid encompassed amino acids 39–182 (pEDA85); the YIF1 hybrid, amino acids 55–314 (pEDA76); and the STT3 hybrid, amino acids 45–720 (pEDA93). G_{BD}–MNN10 (pEDA109) was constructed by digesting pEDA96 with *Eco*RI and *Sal*I and subcloning the MNN10 fragment into pGBT9C. To make MNN10–G_{BD}, a PCR fragment with the MNN10 coding region was cloned into the *Bam*HI site of the C-terminal G_{BD} fusion vector D134 (gift from R. Brazas). The SIR3 and SIR4 overexpression plasmids were pJR104 and pHR643, respectively (from J. Rine's laboratory).

Indirect immunofluorescence and western blot analysis. For immunofluorescence, cells were grown to mid-log phase, fixed with formaldehyde and prepared as described[24]. The primary antibody used was one directed against G_{BD} (Upstate Biotechnology). For western blots, strain YSB35 transformants were grown to an absorbance at 600 nm of 1.0 and lysed by vortexing with glass beads. Western blotting was done as described[25] using the same anti-G_{BD} primary antibody to detect G_{BD} hybrids.

Received 23 March; accepted 16 June 1998.

1. Hecht, A., Laroche, T., Strahl-Bolsinger, S., Gasser, S. M. & Grunstein, M. Histone H3 and H4 N-termini interact with the silent information regulators Sir3 and Sir4: A model for the formation of heterochromatin in yeast. *Cell* **80,** 583–592 (1995).
2. Triolo, T. & Sternglanz, R. Role of interactions between the origin recognition complex and SIR1 in transcriptional silencing. *Nature* **381,** 251–253 (1996).
3. Hecht, A., Strahl-Bolsinger, S. & Grunstein, M. Spreading of transcriptional repression by SIR3 from telomeric heterochromatin. *Nature* **383,** 92–96 (1996).
4. Strahl-Bolsinger, S., Hecht, A., Luo, K. & Grunstein, M. SIR2 and SIR4 interactions in core and extended telomeric heterochromatin in yeast. *Genes Dev.* **11,** 83–93 (1997).
5. Gotta, M. *et al*. The clustering of telomeres and colocalization with Rap1, Sir3, and Sir4 proteins in wild-type *Saccharomyces cerevisiae*. *J. Cell Biol.* **134,** 1349–1363 (1996).
6. Hiraoka, Y., Agard, D. A. & Sedat, J. W. Temporal and spatial coordination of chromosome movement, spindle formation, and nuclear envelope breakdown during prometaphase in *Drosophila melanogaster* embryos. *J. Cell. Biol.* **11,** 2815–2828 (1990).
7. Funabiki, H., Hagan, I., Usawa, S. & Yanagida, M. Cell cycle dependent specific positioning and clustering of centromeres and telomeres in fission yeast. *J. Cell Biol.* **121,** 961–976 (1993).
8. Marshall, W. F., Dernburg, A. F., Harmon, B., Agard, D. A. & Sedat, J. W. Specific interactions of chromatin with the nuclear envelope: Positional determination within the nucleus in *Drosophila melanogaster*. *Mol. Biol. Cell* **7,** 825–842 (1996).
9. Brand, A. H., Breeden, L., Abraham, J., Sternglanz, R. & Nasmyth, K. Characterization of a "silencer" in yeast: A DNA sequence with properties opposite to those of a transcriptional enhancer. *Cell* **41,** 41–48 (1985).
10. Chien, C.-T., Buck, S., Sternglanz, R. & Shore, D. Targeting of SIR1 protein establishes transcriptional silencing at *HM* loci and telomeres in yeast. *Cell* **75,** 531–541 (1993).
11. Buck, S. W. & Shore, D. Action of a RAP1 carboxy-terminal silencing domain reveals an underlying competition between *HMR* and telomeres in yeast. *Genes Dev.* **9,** 370–384 (1995).
12. Marcand, S., Buck, S. W., Moretti, P., Gilson, E. & Shore, D. Silencing of genes at nontelomeric sites in yeast is controlled by sequestration of silencing factors at telomeres by Rap1 protein. *Genes Dev.* **10,** 1297–1309 (1996).
13. Munro, S. Sequences within and adjacent to the transmembrane segment of the α-2,6-sialyltransferase specify Golgi retention. *EMBO J.* **10,** 3577–3588 (1991).
14. Machamer, C. E. *et al*. Retention of a *cis* Golgi protein requires polar residues on one face of a predicted α-helix in the transmembrane domain. *Mol. Biol. Cell* **4,** 695–704 (1993).
15. Dean, N. & Poster, J. Molecular and phenotypic analysis of the *S. cerevisiae MNN10* gene identifies a family of related glycosyltransferases. *Glycobiology* **6,** 73–81 (1996).
16. Zufferey, R. *et al*. STT3, a highly conserved protein required for yeast oligosaccharyl transferase activity *in vivo*. *EMBO J.* **14,** 4949–4960 (1995).
17. Karaoglu, D., Kelleher, D. J. & Gilmore, R. The highly conserved Stt3 protein is a subunit of the yeast oligosaccharyltransferase and forms a subcomplex with Ost3p and Ost4p. *J. Biol. Chem.* **272,** 32513–32520 (1997).
18. Khosravi-Far, R. *et al*. Isoprenoid modifcation of rab proteins terminating in CC or CXC motifs. *Proc. Natl Acad. Sci. USA* **88,** 6264–6268 (1991).
19. Kinsella, B. T. & Maltese, W. A. *rab* GTP-binding proteins with three different carboxyl-terminal cysteine motifs are modified *in vivo* by 20-carbon isoprenoids. *J. Biol. Chem.* **267,** 3940–3945 (1992).
20. Maillet, L. *et al*. Evidence for silencing compartments within the yeast nucleus: a role for telomere proximity and Sir protein concentration in silencer-mediated repression. *Genes Dev.* **10,** 1796–1811 (1996).
21. Stone, E. M., Swanson, M. J., Romeo, A. M., Hicks, J. B. & Sternglanz, R. The *SIR1* gene of *Saccharomyces cerevisiae* and its role as an extragenic suppressor of several mating-defective mutants. *Mol. Cell. Biol.* **11,** 2253–2262 (1991).
22. Renauld, H. *et al*. Silent domains are assembled continuously from the telomere and are defined by promoter distance and strength, and *SIR3* dosage. *Genes Dev.* **7,** 1133–1145 (1993).
23. Ma, J. & Ptashne, M. A new class of yeast transcriptional activators. *Cell* **51,** 113–119 (1987).
24. Pringle, J. R., Adams, A. E. M., Drubin, G. & Haarer, B. K. Guide to yeast genetics and molecular biology. *Meth. Enzymol.* **194,** 565–602 (1991).
25. Harlow, E. & Lane, D. *Antibodies: A Laboratory Manual* (CSHL Press, Cold Spring Harbor, NY, 1988).
26. Kaiser, C. A. & Schekman, R. Distinct sets of *SEC* genes govern transport vesicle formation and fusion early in the secretory pathway. *Cell* **61,** 723–733 (1990).

Supplementary information is available on *Nature*'s World-Wide Web site (http://www.nature.com) or as paper copy from the London editorial office of *Nature*.

Acknowledgements. We thank D. Gallwitz for communicating unpublished results; N. Dean, H. Park, S. Marcand, D. Shore and R. Brazas for plasmids and strains; and N. Dean, A. Mook and C. Dingwall for advice and comments. This work was supported by a grant from the NIH.

Correspondence and requests for materials should be addressed to R.S. (e-mail:rolf@life.bio.sunysb.edu).

Crystal structure of a small heat-shock protein

Kyeong Kyu Kim, Rosalind Kim & Sung-Hou Kim

Physical Biosciences Division of the Lawrence Berkeley National Laboratory and the Department of Chemistry, University of California at Berkeley, 220 Melvin Calvin Laboratory, Berkeley, California 94720-5230, USA

The principal heat-shock proteins that have chaperone activity (that is, they protect newly made proteins from misfolding) belong to five conserved classes: HSP100, HSP90, HSP70, HSP60 and the small heat-shock proteins (sHSPs). The sHSPs can form large multimeric structures and have a wide range of cellular functions, including endowing cells with thermotolerance *in vivo*[1,2] and being able to act as molecular chaperones *in vitro*[3–8]; sHSPs do this by forming stable complexes with folding intermediates of their protein substrates[9,10]. However, there is little information available about these structures or the mechanism by which substrates are protected from thermal denaturation by sHSPs. Here we report the crystal structure of a small heat-shock protein from *Methanococcus jannaschii*, a hyperthermophilic archaeon. The monomeric folding unit is a composite β-sandwich in which one of the β-strands comes from a neighbouring molecule. Twenty-four monomers form a hollow spherical complex of octahedral symmetry, with eight trigonal and six square 'windows'. The sphere has an outer diameter of 120 Å and an inner diameter of 65 Å.

The sHSPs are abundant and ubiquitous in nature; they range in size from 12K to 42K and are found as large complexes of 200K–800K. The sHSPs share a sequence of about 100 residues which is homologous to α-crystallin from the vertebrate eye lens, and is called the α-crystallin domain or small-heat-shock-protein domain. The sHSP from *M. jannaschii* (MjHSP16.5, relative molecular mass 16.5K)[11] also contains an α-crystallin domain composed of 90 residues (Fig. 1, residues 46 to 135). The domain has 20.7% sequence identity with human αA-crystallin and 31.4% identity with rice HSP16.9 (refs 3, 12). The protein forms homogeneous oligomers and has molecular chaperone activity[13]. We have determined the crystal structure of MjHSP16.5 from *M. jannaschii* at 2.9 Å resolution by using single isomorphous replacement and non-crystallographic symmetry (NCS) averaging (Table 1 and Fig. 2).

MjHSP16.5 is a hollow spherical complex composed of 24 subunits generated by a three-fold crystallographic symmetry operation of an asymmetric unit containing eight subunits (Fig. 3a). These eight subunits, in turn, are related by three kinds of NCS: four two-fold, one three-fold, and one four-fold symmetries. Therefore, 24 subunits in the complex are related by an octahedral symmetry, with a total of twelve two-fold, three three-fold, and three four-fold NCS axes, and one three-fold crystallographic symmetry axis[11] (Fig. 3a). The outer diameter of the sphere is ~120 Å, and the inner diameter is ~65 Å (Fig. 3b). The inside of the sphere is hollow and no remarkable electron density is found at the current resolution. There are eight triangular and six square windows on the surface of the sphere.

Each folding unit is composed of nine β-strands in two sheets, two short 3_{10}-helices, and one short β-strand (Fig. 4a). One of the β-strands comes from a neighbouring subunit. The amino-terminal 32 residues are highly disordered, but from residue 33 onwards, including the entire α-crystallin domain (residues 46–135) and